

Deuteration and evolution in the massive star formation process: the role of surface chemistry

F. Fontani¹, G. Busquet^{2,3}, Aina Palau⁴, P. Caselli⁵, Á. Sánchez-Monge⁶, J.C. Tan^{7,8}, and M. Audard⁹

¹ INAF - Osservatorio Astrofisico di Arcetri, L.go E. Fermi 5, I-50125, Firenze, Italy

² Instituto de Astrofísica de Andalucía, CSIC, Glorieta de la Astronomía, E-18008, Granada, Spain

³ INAF - Istituto di Astrofisica e Planetologia Spaziali, via Fosso del Cavaliere 100, I-00133, Roma, Italy

⁴ Centro de Radioastronomía y Astrofísica, Universidad Nacional Autónoma de México, P.O. Box 3-72, 58090 Morelia, Michoacán, México

⁵ Max-Planck-Institut für extraterrestrische Physik (MPE), Giessenbachstr., D-85741 Garching, Germany

⁶ I. Physikalisches Institut der Universität zu Köln, Zùlpicher Strasse 77, 50937 Köln, Germany

⁷ Department of Astronomy, University of Florida, Gainesville, FL 32611, USA

⁸ Department of Physics, University of Florida, Gainesville, FL 32611, USA

⁹ Department of Astronomy, University of Geneva, Ch. d'Ecogia 16, 1290 Versoix

Received date; accepted date

ABSTRACT

Context. An ever growing number of observational and theoretical evidence suggests that the deuterated fraction (column density ratio between a species containing D and its hydrogenated counterpart, D_{frac}) is an evolutionary indicator both in the low- and the high-mass star formation process. However, the role of surface chemistry in these studies has not been quantified from an observational point of view.

Aims. Because many abundant species, like NH_3 , H_2CO and CH_3OH , are actively produced on ice mantles of dust grains during the early cold phases, their D_{frac} is expected to evolve differently from that of species formed only (or predominantly) in the gas, like N_2H^+ , HNC, HCN and their deuterated isotopologues. The differences are expected to be relevant especially after the protostellar birth, in which the temperature rises up causing the evaporation of ice mantles.

Methods. In order to compare how the deuterated fractions of species formed only in the gas and partially or uniquely on grain surfaces evolve with time, we observed rotational transitions of CH_3OH , $^{13}\text{CH}_3\text{OH}$, CH_2DOH , CH_3OD at 3 and 1.3 mm, and of NH_2D at 3 mm with the IRAM-30m telescope, and the inversion transitions (1,1) and (2,2) of NH_3 with the GBT, towards most of the cores already observed by Fontani et al. (2011, 2014) in N_2H^+ , N_2D^+ , HNC, DNC.

Results. NH_2D is detected in all but two cores, regardless of the evolutionary stage. $D_{\text{frac}}(\text{NH}_3)$ is on average above 0.1, and does not change significantly from the earliest to the most evolved phases, although the highest average value is found in the protostellar phase (~ 0.3). Few lines of CH_2DOH and CH_3OD are clearly detected, and only towards protostellar cores or externally heated starless cores. In quiescent starless cores, we have found only one doubtful detection of CH_2DOH .

Conclusions. This work clearly confirms an expected different evolutionary trend of the species formed exclusively in the gas (N_2D^+ and N_2H^+) and those formed partially (NH_2D and NH_3) or totally (CH_2DOH and CH_3OH) on grain mantles. The study also reinforces the idea that $D_{\text{frac}}(\text{N}_2\text{H}^+)$ is the best tracer of massive starless cores, while high values of $D_{\text{frac}}(\text{CH}_3\text{OH})$ seem rather good tracers of the early protostellar phases, at which the evaporation/sputtering of the grain mantles is most efficient.

Key words. Stars: formation – ISM: clouds – ISM: molecules – Radio lines: ISM

1. Introduction

Theory and observations suggest that the abundance of deuterated molecules in dense star-forming cores is related to the core evolution. The formation of deuterated molecules is favoured by the combination of low temperatures ($T \leq 20$ K) and high-densities ($n \geq 10^4 \text{ cm}^{-3}$), which on one hand boosts the depletion of CO and other neutrals, and on the other hand makes the relative abundance between a species containing D and its hydrogenated counterpart (the so-called deuterated fraction, D_{frac}) higher by 3–4 orders of magnitude with respect to the $[\text{D}/\text{H}]$ interstellar abundance ($\sim 10^{-5}$, e.g. Oliveira et al. 2003), due to the endothermicity of their backward reactions (see e.g. Millar et al. 1989, Gerlich et al. 2002). After protostellar birth, the young stellar object formed at the core centre heats up its sur-

rounding material, and the temperature enhancement favours the progressive destruction of deuterated species and, consequently, makes D_{frac} decrease (see e.g. Caselli et al. 2002). Observations of *low-mass star-forming cores* have confirmed this theoretical scenario: both the column density ratio $D_{\text{frac}}(\text{N}_2\text{H}^+)$ and the column density of *ortho*- H_2D^+ , the parent species of most of the deuterated molecules formed in the gas (e.g. DCO^+ , N_2D^+ , DNC), increase in starless cores close to the onset of gravitational collapse, and then, after the formation of the protostar, decrease as the core evolves (Crapsi et al. 2005, Emprechtinger et al. 2009, Caselli et al. 2008). Growing observational evidence suggests that high values of D_{frac} are typical also in high-mass star-forming cores (e.g. Fontani et al. 2006, Pillai et al. 2007, 2011, Miettinen et al. 2011), and that D_{frac} of some species could be an evolutionary indicator also in the intermediate- and high-mass regime (e.g. Busquet et al. 2010, Fontani et al. 2011, Sakai et al. 2012).

Send offprint requests to: F. Fontani, e-mail: fontani@arcetri.astro.it

To investigate the relation between D_{frac} and core evolution in the high-mass regime in a systematic way, our team started a survey of deuterated molecules in about 30 dense cores carefully selected and almost equally divided among the three evolutionary phases in which we can roughly divide observationally the high-mass star formation process (see e.g. Beuther et al. 2007 and Tan et al. 2014): high-mass starless cores (HMSCs), high-mass protostellar objects (HMPOs) and ultracompact HII regions (UCHIIs). In brief, the targets were selected as follows: the HMSCs had to be dense molecular cores not associated with indicators of star formation; the HMPOs had to show outflows, and/or infrared sources, and/or faint ($S_{3.6\text{cm}} < 1\text{mJy}$) radio continuum emission; the UCHIIs had to be associated with stronger ($S_{3.6\text{cm}} \geq 1\text{mJy}$) radio continuum. In selecting the sources, we rejected cores blended with nearby cores to avoid confusion and make the emission of the targeted core dominant.

In the first study, we (Fontani et al. 2011, hereafter paperI) presented the results obtained from spectroscopic observations of millimeter rotational transitions of N_2H^+ and N_2D^+ obtained with the IRAM-30m telescope, where we showed that $D_{\text{frac}}(\text{N}_2\text{H}^+)$ is ~ 0.26 in HMSCs, and drops by about an order of magnitude in the HMPO and UC HII stages. These results are consistent with the fact that deuteration of N_2H^+ starts from the reaction $\text{H}_2\text{D}^+ + \text{N}_2 \rightarrow \text{N}_2\text{D}^+ + \text{H}_2$, efficient only at temperatures $\leq 20\text{ K}$ (Gerlich et al. 2002). In a following study, focused on DNC/HNC, Fontani et al. (2014, paperII) showed that $D_{\text{frac}}(\text{HNC})$ also decreases from the pre- to the proto-stellar phase, but much more moderately, indicating that the ratio N_2D^+ -to- N_2H^+ is more appropriate to identify massive starless cores. This is consistent with the prediction that DNC can also easily form when the gas gets warmer, because the route reaction for the deuteration of HNC is linked to CH_2D^+ , which can stay abundant up to temperatures of 70 K (e.g. Leurini et al. 2006). However, N_2H^+ , HNC and their deuterated isotopologues can form mainly (HNC, DNC) or solely (N_2H^+ , N_2D^+) in the gas phase. Other important molecules, like NH_3 , H_2CO , CH_3OH and their deuterated forms, can be produced on dust grain surfaces (e.g. Aikawa et al. 2005), and theoretical models show that this can make relevant differences in their D_{frac} , especially during the protostellar phase in which grain mantles evaporate (Aikawa et al. 2012).

In this work we investigate the role of surface chemistry by means of measurements of $D_{\text{frac}}(\text{NH}_3)$ and $D_{\text{frac}}(\text{CH}_3\text{OH})$. Because methanol and its deuterated forms can be produced *only on grain surfaces* (see e.g. Parise et al. 2002, Garrod et al. 2007), $D_{\text{frac}}(\text{N}_2\text{H}^+)$ and $D_{\text{frac}}(\text{CH}_3\text{OH})$ represent the two "extreme conditions" under which deuteration can occur: on grain surfaces only (CH_3OH) and in gas only (N_2H^+). Therefore, the results obtained in this work and in paperI can be used as reference for the deuteration process of any other species formed potentially both in the gas and on dust grains. In Sect. 2 we present the source sample and give an overview of the technical details of the observations. The main results are presented and discussed in Sects. 3 and 4, respectively. A summary with the main conclusions of the work is given in Sect. 5.

2. Source list, observations and data reduction

2.1. Source list

We targeted the same sources studied in paperI, to avoid possible biases due to the source selection when comparing the deuterated fractions. Table 1 contains the list of the observed sources selected as explained briefly in Sect. 1. In particular,

three HMSCs have been classified as "warm" cores because they show evidence of heating from external sources (see paperI for details). More information extracted from the literature about the star forming regions in which the sources lie are given in Table A.1 of paperI. To the list of HMSCs reported in paperI, we have added the source G028-C3, selected applying the same selection criteria as for the other HMSCs.

2.2. IRAM-30m observations

Run-1: towards all sources in Table 1, observations of the *ortho*- and *para*- $\text{NH}_2\text{D}(1_{1,1} - 1_{0,1})$ line were obtained simultaneously to the N_2D^+ and N_2H^+ observations described in paperI. Table 2 lists the main observational parameters. We refer to Sect. 2 of paperI for any other technical detail related to these observations.

Run-2: we performed CH_3OH and CH_2DOH observations towards all sources observed in paperI from the 6th to the 9th of February, 2013. We observed simultaneously two bands at 3 and 1.3 mm, covering some important rotational transitions of CH_3OH , $^{13}\text{CH}_3\text{OH}$ and CH_2DOH . Table 2 presents the observed spectral windows and some main technical observational parameters. The atmospheric conditions were very stable during the whole observing period, with precipitable water vapour usually below $\sim 2\text{ mm}$. The observations were made in wobbler-switching mode. Pointing was checked almost every hour on nearby quasars or bright HII regions. The data were calibrated with the chopper wheel technique (see Kutner & Ulich 1981), with a calibration uncertainty of $\sim 20\%$. The spectra were obtained in antenna temperature units, T_A^* , and then converted to main beam brightness temperature, T_{MB} , via the relation $T_A^* = T_{\text{MB}}(B_{\text{eff}}/F_{\text{eff}})$. The spectra were obtained with the Fast Fourier Transform Spectrometers (FTS), providing a broad band of $\sim 8\text{ GHz}$ simultaneously at 3 and 1.3 mm (see Table 2 for details). All calibrated spectra were analyzed using the GILDAS¹ software developed at the IRAM and the Observatoire de Grenoble. The rest frequencies used for the line identification have been taken from the Cologne Molecular Database for Spectroscopy (CDMS, <http://www.astro.uni-koeln.de/cdms>; Müller et al. 2001, 2005).

2.3. GBT observations

The ammonia (1,1) and (2,2) inversion transitions (rest frequencies 23.6944955 and 23.7226336 GHz, respectively) were observed with the 100 m Robert C. Byrd Green Bank Telescope² (GBT) during the 13th and 21st March and the 4th and 21th April 2013. The GBT spectrometer backend was configured to simultaneously observe the two transitions in separate spectral windows, using bands of 50 MHz and spectral resolution of 12.2070 kHz, corresponding to 0.154 km s^{-1} for both lines. The main observational parameters are listed in Table 2. The data were taken using in-band frequency switching with a throw of 7.5 MHz. The beam FWHM was approximately $32''$. The pointing was checked at hourly intervals on a nearby quasar, with corrections approximately $2''$ – $3''$. Flux calibration was performed on 3C123 and NGC7027. The absolute flux accuracy is 10–20%. Data re-

¹ The GILDAS software is available at <http://www.iram.fr/IRAMFR/GILDAS>

² The National Radio Astronomy Observatory is a facility of the National Science Foundation operated under cooperative agreement by Associated Universities, Inc.

Table 1. List of the observed sources. Col. 4 shows the velocity at which we centred the spectra, corresponding to the systemic velocity. More information (e.g. source distances, bolometric luminosities of the associated star forming regions, reference papers) are given in Table 1 of paperI.

source	RA(J2000) h m s	Dec(J2000) ° ′ ″	V_{LSR} km s ⁻¹
HMSC			
I00117-MM2	00:14:26.3	+64:28:28	-36.3
AFGL5142-EC ^w	05:30:48.7	+33:47:53	-3.9
05358-mm3 ^w	05:39:12.5	+35:45:55	-17.6
G034-G2(MM2)	18:56:50.0	+01:23:08	+43.6
G034-F2(MM7)	18:53:19.1	+01:26:53	+57.7
G034-F1(MM8)	18:53:16.5	+01:26:10	+57.7
G028-C1(MM9)	18:42:46.9	-04:04:08	+78.3
G028-C3(MM11) ^a	18:42:44	-04:01:54	+78.3
I20293-WC	20:31:10.7	+40:03:28	+6.3
I22134-G ^w	22:15:10.5	+58:48:59	-18.3
I22134-B	22:15:05.8	+58:48:59	-18.3
HMPO			
I00117-MM1	00:14:26.1	+64:28:44	-36.3
I04579-VLA1	05:01:39.9	+47:07:21	-17.0
AFGL5142-MM	05:30:48.0	+33:47:54	-3.9
05358-mm1	05:39:13.1	+35:45:51	-17.6
18089-1732	18:11:51.4	-17:31:28	+32.7
18517+0437	18:54:14.2	+04:41:41	+43.7
G75-core	20:21:44.0	+37:26:38	+0.2
I20293-MM1	20:31:12.8	+40:03:23	+6.3
I21307	21:32:30.6	+51:02:16	-46.7
I23385	23:40:54.5	+61:10:28	-50.5
UC HII			
G5.89-0.39	18:00:30.5	-24:04:01	+9.0
I19035-VLA1	19:06:01.5	+06:46:35	+32.4
19410+2336	19:43:11.4	+23:44:06	+22.4
ON1	20:10:09.1	+31:31:36	+12.0
I22134-VLA1	22:15:09.2	+58:49:08	-18.3
23033+5951	23:05:24.6	+60:08:09	-53.0
NGC7538-IRS9	23:14:01.8	+61:27:20	-57.0

Notes. ^(a) Source not included in paperI, selected from Butler & Tan (2009). See also Butler et al. (2014); ^(w) "warm" ($T \geq 20$ K) HMSCs externally heated (see paperI).

duction and calibrations were done using the GBTIDL³ package, and subsequently converted to CLASS format.

3. Results and derivation of physical parameters

3.1. NH_3 and NH_2D

3.1.1. Detection summary and parameters derived directly from the fits

NH_3 : the $\text{NH}_3(1,1)$ and $(2,2)$ inversion lines have been detected with excellent signal-to-noise ratio in all sources observed. The spectra of all HMSCs, HMPOs and UC HII are shown in Figs. A-1, A-2 and A-3, respectively, of Appendix-A. Both transitions consist of 18 hyperfine components, grouped in 5 lines: the main one at the center of the spectrum, and four satellites

symmetrically placed in frequency with respect to the main one (see Ho & Townes 1983 for details). The spectra have been fit considering this hyperfine structure when the satellites are detected. When they are not, we adopted a simplified approach in which we fitted the main line with a Gaussian curve. This simplified method was used for 8 of the $(2,2)$ spectra observed, in which the satellites have not been detected. The fit procedure has given good results (with very low residuals, see Figs. A-1, A-2 and A-3) using both methods. The simplified approach in principle tends to overestimate the intrinsic line width, as the main line is in reality a blending of several hyperfine components. To quantify this, we have taken a $(2,2)$ spectrum with hyperfine structure nicely fit (one spectrum per evolutionary group), applied the simplified method and compared the derived line width with that obtained from the accurate method (the hyperfine fit method). From this comparison, we quantify an overestimate of at most the 10% of the true intrinsic line width. Nevertheless, because the column density in this approach is computed from the integral of the line (see Sects. 3.1.2 and 3.1.3), this overestimation does not influence the calculation of neither the column density nor the deuterated fraction.

The line parameters derived from these fit procedures are listed in Tables 3 and 4. The accurate method has given a well-constrained value of the optical depth of the main component of the $(1,1)$ line ($\tau_m(1,1)/\Delta\tau_m(1,1) \geq 3$) for all objects except for I04579-VLA1, for which the line is optically thin. The average $\tau_m(1,1)$ is ~ 1 , with no significant differences between the three evolutionary groups, while $\tau_m(2,2)$ is usually smaller than 1. The average line widths of the $(1,1)$ lines are ~ 1.7 , ~ 2.3 and ~ 2.6 km s⁻¹ for the HMSC, HMPO and UC HII groups (standard deviation 0.5, 0.6 and 0.7 km s⁻¹, respectively), and tend to increase with evolution, as expected (Sánchez-Monge et al. 2013).

NH_2D : the *ortho*- $\text{NH}_2\text{D}(1_{1,1} - 1_{0,1})$ line has been detected in all sources observed except in two HMPOs (I04579-VLA1 and I21307). The detection rate is thus $\sim 92\%$. The *para*- $\text{NH}_2\text{D}(1_{1,1} - 1_{0,1})$ line has been detected in 13 out of 26 sources observed (detection rate of 50%). The spectra of both lines are shown in Figs. A-4 and A-5. In this work we will use the *ortho*- $\text{NH}_2\text{D}(1_{1,1} - 1_{0,1})$ line to derive the physical parameters of our interest because of its higher detection rate and signal-to-noise ratio. The line of the *para*-species will be used to test whether the *ortho*-/*para*-ratio assumed to derive the total column density in Sect. 3.1.3 is correct. Like ammonia, the NH_2D lines have been fit taking into account their hyperfine structure driven by the quadrupole moment of the Deuterium and Nitrogen nuclei (see Olberg et al. 1985 for details).

In general, the procedure has provided good fits to the spectra, except a few cases in which deviations from the LTE (symmetric) pattern are seen (e.g. G028-C1, I20293-WC, I20293-MM1, 23033+5951, see Fig. A-4). To check if (and how) our simplified LTE approach gives results different from those of a non-LTE analysis, we have run the non-LTE radiative transfer code RADEX⁴ (Van der Tak et al. 2007) in order to reproduce the measured line ratios of the two lines (*ortho*- NH_2D and *para*- NH_2D). The molecular data were taken from the LAMDA database (Schöier et al. 2005) using the collisional rate coefficients with H_2 of Daniel et al. (2014). We built grids of models with kinetic temperatures in the range 8 – 25 K, H_2 volume densities in the range $10^3 - 10^8$ cm⁻³, and total column densities of $10^{12} - 10^{15}$ cm⁻². We assumed line widths of 1.5 km s⁻¹ and an *ortho*-to-*para*-ratio of 3. The 'best estimate' of the col-

³ GBTIDL is an interactive package for reduction and analysis of spectral line data taken with the GBT. See <http://gbtidl.nrao.edu/>

⁴ <http://www.sron.rug.nl/~vdtak/radex/>

Table 2. Observed transitions and technical parameters

molecular line	line rest frequency (GHz)	HPBW ($''$)	$\Delta\nu$ (km s $^{-1}$)	T_{sys} K	η_{MB}
IRAM-30m Telescope					
<i>ortho</i> -NH $_2$ D(1 $_{1,1}$ – 1 $_{0,1}$)	85.9263	~ 28	0.136	$\sim 85 - 120$	0.85
<i>para</i> -NH $_2$ D(1 $_{1,1}$ – 1 $_{0,1}$)	110.1536	~ 22	0.106	$\sim 95 - 125$	0.83
CH $_3$ OH(3mm-band)	89.11 – 96.89 ^a	27 ^b	$\sim 0.62^c$	$\sim 100 - 120$	0.84
CH $_3$ OH(1mm-band)	216.0 – 223.78 ^a	11 ^b	$\sim 0.26^c$	$\sim 200 - 300$	0.66
Green Bank Telescope					
NH $_3$ (1,1)	23.6945	~ 32	~ 0.15	$\sim 50 - 100$	~ 0.81
NH $_3$ (2,2)	23.7226	~ 32	~ 0.15	$\sim 50 - 100$	~ 0.81

Notes. ^(a) Total spectral window covered by the FTS correlator. Please see Tables B-1 and B-2 to see the transitions detected in it. ^(b) Telescope HPBW at the central frequency of the spectral window. ^(c) Maximum spectral resolution obtained with FTS.**Table 3.** Derived line parameters of NH $_3$ (1,1). All lines have been fit taking into account the hyperfine structure as explained in Sect. 3.1.1. Cols. 2–5 report the output parameters of the fitting procedure ($A \times \tau_m = f[J_v(T_{\text{ex}}) - J_v(T_{\text{BG}})]$, where f is the filling factor, assumed to be unity, $J_v(T_{\text{ex}})$ and $J_v(T_{\text{BG}})$ are the equivalent Rayleigh-Jeans excitation and background temperatures, respectively, and τ_m is the opacity of the main group of hyperfine components; V_{peak} = peak velocity; $\Delta\nu$ = full width at half maximum corrected for hyperfine splitting; τ_m = opacity of the main group of hyperfine components) for the (1,1) line, and Col. 6 lists the excitation temperature of the transition derived as explained in Sect. 3.1.2. The uncertainties obtained from either the fitting procedure (parameters in Cols. 2 – 5) or from the propagation of errors (Col. 6) are in parentheses.

source	$A \times \tau_m(1, 1)$	$V_{\text{peak}}(1, 1)$ (km s $^{-1}$)	$\Delta\nu(1, 1)$ (km s $^{-1}$)	$\tau_m(1, 1)$	$T_{\text{ex}1,1}$ (K)
HMSCs					
I00117–MM2	1.83(0.06)	–36.16(0.01)	1.71(0.03)	0.71(0.09)	15(4)
AFGL5142–EC	3.69(0.03)	–2.936(0.004)	2.44(0.01)	0.77(0.02)	7.4(0.2)
05358–mm3	5.32(0.01)	–16.258(0.004)	1.989(0.005)	0.85(0.01)	8.86(0.07)
G034–G2	3.68(0.04)	41.854(0.007)	2.25(0.01)	1.52(0.04)	5.0(0.1)
G028–C1	2.69(0.01)	79.810(0.007)	2.30(0.01)	2.50(0.07)	3.67(0.05)
G028–C3	2.89(0.08)	80.858(0.007)	1.15(0.02)	1.9(0.1)	4.1(0.2)
I20293–WC	5.46(0.02)	6.419(0.004)	2.080(0.006)	1.31(0.01)	6.76(0.07)
I22134–G	2.41(0.07)	–18.643(0.006)	1.33(0.02)	0.40(0.07)	9(2)
I22134–B	1.72(0.08)	–18.800(0.01)	1.15(0.03)	0.6(0.1)	5.4(0.9)
HMPOs					
I00117–MM1	1.59(0.03)	–36.32(0.01)	1.59(0.04)	0.13(0.03)	5.2(0.6)
I04579–VLA1	0.272(0.01)	–16.73(0.03)	1.73(0.07)	0.1 ^e	\sim ^f
AFGL5142–MM	3.524(0.001)	–3.072(0.002)	2.644(0.007)	0.75(0.01)	7.28(0.01)
05358–mm1	4.636(0.003)	–16.318(0.003)	2.064(0.001)	0.80(0.01)	8.39(0.02)
18089–1732 ^c	8.301(0.006)	33.02(0.01)	3.241(0.004)	2.53(0.01)	5.9(0.1)
18517+0437	1.76(0.03)	43.908(0.009)	2.52(0.03)	0.43(0.04)	6.7(0.7)
G75–core	2.99(0.04)	0.067(0.009)	3.42(0.02)	0.50(0.03)	8.6(0.6)
I20293–MM1	8.40(0.04)	6.058(0.003)	1.739(0.004)	1.15(0.02)	9.9(0.2)
I21307	0.61(0.05)	–46.57(0.04)	1.9(0.1)	0.8(0.2)	3.4(0.5)
I23385 ^d	0.84(0.03)	–50.21(0.03)	2.09(0.08)	0.15(0.05)	8(5)
UC H $_{\text{IIS}}$					
G5.89–0.39	5.63(0.02)	8.70(0.01)	3.745(0.002)	0.65(0.01)	11.2(0.1)
I19035–VLA1	1.90(0.03)	32.56(0.01)	3.64(0.03)	1.08(0.05)	4.4(0.2)
19410+2336	12.054(0.005)	22.458(0.001)	1.389(0.001)	1.05(0.01)	14.12(0.02)
ON1	13.25(0.02)	10.985(0.001)	2.886(0.005)	1.58(0.01)	10.98(0.02)
23033+5951	4.96(0.07)	–53.444(0.006)	1.95(0.02)	0.98(0.04)	7.7(0.4)
NGC7538–IRS9	3.94(0.04)	–57.31(0.01)	2.17(0.03)	1.00(0.01)	6.54(0.08)

Notes. ^(a) Integrated area of the main group of hyperfine components, in K km s $^{-1}$; ^(b) Peak intensity of the main group of hyperfine components, in K; ^(c) The spectrum shows two velocity components (Fig. A-2). Only the fit to the stronger component is shown; ^(d) The spectrum shows two velocity components (Fig. A-2). Fontani et al. (2004) also found these two components in C 18 O and attributed the one centred at ~ -50 km s $^{-1}$ to the HMPO. Only the fit to this component is shown. ^(e) derived from the hyperfine fit procedure; ^(f) an average value of 6.5 K, computed from the HMPOs with well-constrained opacity, is assumed.

Table 4. Same as Table 3 for the NH_3 (2,2) transitions. For the sources with 'HFS' in Col. 2, the line hyperfine structure has been fit and the same output parameters in Cols. 2–6 of Table 3 are given in Cols. 3, 5, 6, 7, 9. For the sources with 'G' in Col. 2, the satellites of the (2,2) line are undetected, so that the main group of hyperfine components has been fit with a single Gaussian. For these objects, we give integrated area (in K km s^{-1} , Col. 4) and peak intensity (in K, Col. 8) of this Gaussian, respectively. For the sources marked with a 'T' in Col. 2, we clearly detect the satellites in the (2,2) transition, and performed a good fit to the hyperfine structure, but the line is optically thin. Hence, in Col. 8 we also give the peak temperature of the main group of hyperfine components, which is the parameter used to derive the NH_3 total column density in this case (see Sect. 3.1.2). The uncertainties of all parameters are in parentheses.

		$A \times \tau_m(2,2)$	$\int T_{\text{MB}} dv^a$ (K km s^{-1})	$V_{\text{peak}}(2,2)$ (km s^{-1})	$\Delta v(2,2)$ (km s^{-1})	$\tau_m(2,2)$	$T_{\text{peak}2,2}^b$ (K)	$T_{\text{ex}2,2}$ (K)
HMSCs								
I00117-MM2	G		0.91(0.04)	-36.36(0.04)	1.82(0.09)		0.47(0.04)	— ^e
AFGL5142-EC	HFS	1.73(0.06)		-2.972(0.007)	2.73(0.03)	0.21(0.07)		11(4)
05358-mm3	T	2.31(0.01)		-16.283(0.005)	2.23(0.01)	0.1	2.15(0.05)	— ^e
G034-G2	T	0.67(0.02)		41.56(0.02)	2.16(0.06)	0.1	0.71(0.03)	— ^e
G028-C1	HFS	0.57(0.07)		79.72(0.03)	2.22(0.09)	1.3(0.3)		3.0(0.3)
G028-C3	G		0.40(0.03)	80.87(0.04)	1.4(0.1)		0.27(0.02)	— ^e
I20293-WC	HFS	1.8(0.1)		6.34(0.02)	2.29(0.05)	0.6(0.2)		5(1)
I22134-G	G		1.30(0.04)	-18.81(0.02)	1.50(0.05)		0.81(0.03)	— ^e
I22134-B	G		0.55(0.04)	-18.93(0.05)	1.5(0.1)		0.35(0.02)	— ^e
HMPOs								
I00117-MM1	G		0.97(0.04)	-36.48(0.03)	1.67(0.08)		0.54(0.04)	— ^e
I04579-VLA1	G		0.25(0.02)	-16.85(0.08)	1.9(0.2)		0.12(0.05)	— ^e
AFGL5142-MM	HFS	1.80(0.06)		-3.083(0.003)	2.79(0.03)	0.34(0.07)		8(1)
05358-mm1	T	2.078(0.008)		-16.334(0.001)	2.27(0.01)	0.1	1.96(0.05)	— ^e
18089-1732 ^c	HFS	5.58(0.03)		32.85(0.01)	3.14(0.02)	2.48(0.02)		4.9(0.1)
18517+0437	HFS	0.94(0.07)		43.77(0.02)	2.58(0.07)	0.24(0.08)		7(3)
G75-core	T	1.91(0.02)		-0.12(0.01)	3.76(0.03)	0.1	1.88(0.05)	— ^e
I20293-MM1	HFS	2.6(0.1)		5.901(0.008)	2.01(0.04)	0.2(0.07)		20(5)
I21307	G		0.57(0.04)	-46.71(0.08)	2.35(0.21)		0.23(0.02)	— ^e
I23385 ^d	G		0.82(0.09)	-50.5(0.1)	1.9(0.2)		0.42(0.03)	— ^e
UC Hns								
G5.89-0.39	T	3.62(0.01)		8.772(0.004)	4.519(0.003)	0.1	3.65(0.05)	— ^e
I19035-VLA1	HFS	0.79(0.07)		32.53(0.03)	3.9(0.1)	0.7(0.2)		3.7(0.7)
19410+2336	T	4.22(0.02)		22.306(0.002)	1.65(0.01)	0.1	3.82(0.05)	— ^e
ON1	HFS	6.1(0.1)		10.941(0.007)	3.09(0.02)	0.82(0.05)		10.2(0.8)
23033+5951	T	1.31(0.02)		-53.69(0.02)	2.36(0.03)	0.1	1.22(0.02)	— ^e
NGC7538-IRS9	T	1.57(0.02)		-57.47(0.02)	2.53(0.04)	0.1	1.62(0.03)	— ^e

Notes. ^(a) Integrated area of the main group of hyperfine components, in K km s^{-1} ; ^(b) Peak intensity of the main group of hyperfine components, in K; ^(c) The spectrum shows two velocity components (Fig. A-2). Only the fit to the stronger component is shown; ^(d) The spectrum shows two velocity components (Fig. A-2). Fontani et al. (2004) also found these two components in C^{18}O and attributed the one centred at $\sim -50 \text{ km s}^{-1}$ to the HMPO. Only the fit to this component is shown. ^(e) $T_{\text{ex}2,2}$ cannot be estimated. For these objects, in the calculations described in Sect. 3.1.2 we have assumed $T_{\text{ex}2,2} = T_{\text{ex}1,1}$.

umn densities that we find are roughly consistent with the values measured from the LTE approach, but since we only have one line ratio, we cannot discriminate properly between the different non-LTE models. Therefore, with only one line ratio, all we can say is that the column densities of NH_2D derived assuming LTE conditions are consistent with the values expected from a non-LTE approach.

The average optical depth of the main hyperfine component derived from this fitting procedure is ~ 1 in all three evolutionary groups. For the sources for which the mentioned fitting procedure did not give good results (because of poor signal-to-noise ratio), we have fit the lines with Gaussians. As for the NH_3 lines, this simplified method could overestimate the line widths by at most $\sim 10\%$, and we find yet an increasing trend of the line widths going from the HMSC phase to the HMPO and UC

HII phases, for which mean values (and standard deviations) are: 1.4(0.6), 2.5(1.3) and 2.4(1) km s^{-1} , respectively. All line parameters are listed in Table 5.

3.1.2. NH_3 rotation temperature and total column density

From the $\text{NH}_3(1,1)$ and (2,2) line parameters, we have obtained rotation temperatures, T_{rot} , adopting two methods: for the nine sources having $\tau_{(2,2)}/\Delta\tau_{(2,2)} \geq 3$ and $\tau_{(2,2)} > 0.1$, we have derived first the excitation temperature of the (1,1) and (2,2) lines ($T_{\text{ex}1,1}$ and $T_{\text{ex}2,2}$, respectively) independently using Eq. A.2 of Busquet et al. (2009), and, from these, the column densities of the two levels, $N_{(2,2)}$ and $N_{(1,1)}$, from the relations given in Anglada et al. (1995). Note that, although Eq. A.2 in Busquet et al. (2009) is derived for the (1,1) line, it is valid also for the (2,2) line given

Table 5. Derived line parameters of *ortho*-NH₂D(1_{1,1} – 1_{0,1}) for all sources observed in this line. The spectra of the sources marked with a ‘HFS’ in Col. 2 have been fit taking into account the hyperfine structure as described in Sect. 3.1.1. For these, cols. 3, 5, 6 and 7 give: $A \times \tau_m$, peak velocity, line width and τ_m , respectively (see Table 3). Col. 9 lists the excitation temperatures computed as explained in Sect. 3.1.3. The sources marked with a G in Col. 2 have optically thin lines or not well-constrained opacity. These have been fit with a Gaussian function, so that Cols. 4 and 8 represent total integrated area ($\int T_{\text{MB}} dv$, in K km s⁻¹) and peak intensity (T_{peak} , in K) of this Gaussian, respectively. The uncertainties obtained from either the fitting procedure (parameters in Cols. 3 – 8) or from the propagation of errors (Col. 9) are in parentheses.

source		$A \times \tau_m$	$\int T_{\text{MB}} dv$ (K km s ⁻¹)	V_{peak} (km s ⁻¹)	Δv (km s ⁻¹)	τ_m	T_{peak} (K)	T_{ex} (K)
HMSC								
I00117–MM2	HFS	0.15(0.02)		–35.54(0.08)	2.1(0.2)	0.44(0.16)		7.1(0.1)
AFGL5142–EC	HFS	0.51(0.03)		–2.54(0.03)	1.92(0.07)	0.8(0.1)		7.9(0.1)
05358–mm3	HFS	0.32(0.04)		–16.04(0.05)	1.29(0.09)	1.2(0.4)		6.9(0.06)
G034–G2(MM2)	HFS	0.22(0.01)		41.74(0.03)	1.01(0.07)	0.83(0.03)		6.94(0.01)
G034–F2(MM7)	HFS	0.19(0.02)		58.12(0.03)	1.30(0.07)	0.6(0.2)		7.1(0.1)
G034–F1(MM8)	G		0.36(0.04)	56.3(0.03)	0.6(0.1)		0.08(0.01)	– ^b
G028–C1(MM9)	G		0.75(0.04)	80.20(0.08)	2.8(0.1)		0.13(0.01)	– ^b
G028–C3(MM11)	G		0.114(0.02)	81.07(0.07)	0.9(0.2)		0.04(0.01)	– ^b
I20293–WC	HFS	1.25(0.03)		7.15(0.01)	1.28(0.02)	2.06(0.09)		7.84(0.04)
I22134–G	G		0.20(0.03)	–18.5(0.1)	1.5(0.2)		0.05(0.01)	– ^b
I22134–B	G		0.25(0.03)	–18.95(0.04)	0.86(0.09)		0.15(0.02)	– ^b
HMPO								
I00117–MM1	G		0.39(0.03)	–35.94(0.14)	2.6(0.6)		0.07(0.01)	– ^b
I04579–VLA1			$\leq 0.10^a$	–	–	–	–	–
AFGL5142–MM	HFS	0.51(0.03)		–2.867(0.002)	2.25(0.07)	0.9(0.1)		7.77(0.08)
05358–mm1	HFS	0.14(0.03)		–16.07(0.07)	1.6(0.2)	0.4(0.1)		7.2(0.2)
18089–1732	HFS	0.89(0.06)		34.44(0.04)	1.60(0.07)	2.0(0.2)		7.40(0.05)
18517+0437	HFS	0.12(0.02)		43.9(0.1)	2.2(0.3)	1.1(0.4)		6.52(0.03)
G75–core	G		0.31(0.03)	–1.3(0.5)	5.7(1.7)		0.04(0.01)	– ^b
I20293–MM1	HFS	0.708(0.006)		5.69(0.02)	1.63(0.02)	0.68(0.03)		8.97(0.08)
I21307			$\leq 0.08^a$	–	–		–	–
I23385 ^c	G		0.15(0.02)	–49.4(0.3)	2.7(0.7)		0.03(0.01)	– ^b
UC HII								
G5.89–0.39	HFS	0.15(0.03)		7.9(0.2)	2.2(0.2)	1.8(0.5)		6.45(0.02)
I19035–VLA1	G		0.64(0.03)	32.7(0.2)	4.1(0.5)		0.09(0.01)	– ^b
19410+2336	HFS	0.59(0.02)		22.72(0.01)	1.51(0.02)	0.53(0.07)		9.2(0.2)
ON1	HFS	0.19(0.02)		11.01(0.06)	3.2(0.2)	0.50(0.15)		7.3(0.1)
I22134–VLA1	G		0.12(0.02)	–18.86(0.07)	1.1(0.2)		0.05(0.02)	– ^b
23033+5951	HFS	0.30(0.02)		–53.28(0.03)	1.36(0.06)	0.6(0.2)		7.5(0.1)
NGC7538–IRS9 ^c	G		0.16(0.03)	–56.9(0.4)	3(1)		0.03(0.01)	– ^b

Notes. ^(a) Upper limit to the integrated line intensity from the equation $\int T_{\text{MB}} dv = \frac{\Delta v}{2\sqrt{\ln 2/\pi}} T_{\text{MB}}^{\text{peak}}$, assuming the 3σ rms level of the spectrum as $T_{\text{MB}}^{\text{peak}}$, and an average value of Δv from the other sources; ^(b) T_{ex} cannot be derived from the fit results, therefore the average value of the sources with well-constrained opacity (7.5 K) is assumed; ^(c) marginal detection.

the small difference in frequency between the two transitions. Then, the rotation temperature has been derived from the relation:

$$T_{\text{rot}} = \frac{-41.5}{\ln[(3/5)(N_{(2,2)}/N_{(1,1)})]} \quad (1)$$

For sources with an optically thin (2,2) line, or with $\tau_{(2,2)}$ not determined because the satellites are undetected, $T_{\text{ex},2,2}$ is assumed to be equal to $T_{\text{ex},1,1}$. This hypothesis is justified by the good agreement between the two excitation temperatures in the sources in which they can both be measured (see Sect. 4.2). Under this assumption, we have applied eq. A.4 in Busquet et al. (2009), which utilises the peak intensity of the main hyperfine component of the (2,2) line.

In both methods, the total NH₃ column density, $N(\text{NH}_3)$, has been calculated from Eq. A.6 in Busquet et al. (2009). Both T_{rot} and $N(\text{NH}_3)$ are listed in Table 7. Rotation temperatures range from 11.7 to 29 K, and on average they are ~ 17 , ~ 22 and ~ 22

K for HMSCs, HMPOs and UC HII, respectively (standard deviations are 2.6, 3.5 and 4 K, respectively). Separately, quiescent and “warm” HMSCs have mean temperatures of 16 and 20 K (standard deviations of 2.6 and 1.2 K, respectively), which confirms the higher gas temperature in the “warm” cores. Total NH₃ column densities range from 5.6×10^{13} to $3.6 \times 10^{15} \text{ cm}^{-2}$, and the average values are 9.4×10^{14} , 9.3×10^{14} and $1.6 \times 10^{15} \text{ cm}^{-2}$ in the HMSC, HMPO and UC HII groups, respectively. We have assumed a unity filling factor because available VLA interferometer ammonia maps of some of the targets show that the ammonia emission is extended and fills most of the GBT beam. Nevertheless, we stress that the emission from the target cores is clearly dominant with respect to that of nearby condensations (see Sanchez-Monge et al. 2013).

3.1.3. NH_2D total column density

The NH_2D column densities have been computed from the line parameters of the *ortho*- NH_2D line following Eq. (1) in Busquet et al. (2010), which assumes the same T_{ex} for all the hyperfine components. T_{ex} was computed as described in Sect. 3.1.2 for sources with opacity of the main component well-constrained. For the others, we have assumed $T_{\text{ex}} = 7.5$ K, which is the average value derived from the sources with well-constrained opacity, and obtained the column density from Eq. (A4) of Caselli et al. (2002b), valid for optically thin lines.

Again, we have assumed a unity filling factor because there are few high angular resolution observations of this line towards the targets from which the emitting region of NH_2D can be determined. This assumption is critical, as the *ortho*- NH_2D line has a critical density of $\sim 10^6 \text{ cm}^{-3}$, higher than that of the inversion transitions of NH_3 ($\sim 10^{3-4} \text{ cm}^{-3}$). However, while by neglecting the beam dilution the absolute values of the column densities can be certainly affected, the evolutionary trend of the column density ratio should not be affected by this assumption because the beam dilution is expected to be almost constant, and thus it should introduce only a systematic correction (see also paper I). Also, observations at high angular resolution towards massive star forming regions (Busquet et al. 2010, Pillai et al. 2011) indicate that the emission of NH_2D can be as extended as that of NH_3 , despite the different critical density. For example, the emitting region of $\text{NH}_2\text{D}(1_{1,1} - 1_{0,1})$ and $\text{NH}_3(1,1)$ in I20293-WC and I20293-MM1, both included in our survey, is approximately the same (Busquet et al. 2010). $N(\text{NH}_2\text{D})$ is listed in Table 7.

3.2. Methanol and deuterated methanol lines

In this work we focus the attention on the deuterated fraction of CH_3OH , and on the physical quantities relevant to derive it (i.e. temperature and total column density). Therefore, in what follows we will present the approach adopted to identify the lines from which $D_{\text{frac}}(\text{CH}_3\text{OH})$ will be derived (Sect. 3.2.1), the method to compute rotation temperature and total column density from the line parameters (Sect. 3.2.2), and the deuterated fraction in the sources detected in CH_2DOH (Sect. 4.4).

3.2.1. Lines detected and fit procedure

Multiple CH_3OH lines are detected in the observed spectral windows (Col. 1 of Table 2) towards all sources, while $^{13}\text{CH}_3\text{OH}$ lines are clearly detected in four HMSCs, seven HMPOs and six UC HII regions. CH_2DOH lines are detected only towards 6 objects: three HMSCs and three HMPOs, and two out of the three HMSCs are “warm” cores (see Sect. 2). Moreover, in two HMPOs (AFGL5142-MM and 18089-1732), the $\text{CH}_3\text{OD}(5_{1,5} - 4_{1,4}\text{A}++)$ line at 1.3 mm has been detected, although in 18089-1732 this could be blended with emission of $(\text{CH}_2\text{OH})_2$. Tables B-1 and B-2 give the line parameters obtained from Gaussian fits to the lines detected at the 3σ level and not probably blended with other transitions.

The detection of the deuterated lines has been double-checked by comparing observed and synthetic spectra. For this purpose, the observed spectra were smoothed to 1.0 km s^{-1} at 1 mm and to 2.5 km s^{-1} at 3 mm, to improve the signal-to-noise ratio. The CH_2DOH synthetic spectra were computed assuming LTE and optically thin emission as in Palau et al. (2011), and using the molecular data from the Jet Propulsion Laboratory (Pickett et al. 1998). To build the synthetic spectra, we adopted a line width of 1.5 km s^{-1} at 1 mm and 2.5 km s^{-1} at 3 mm, and

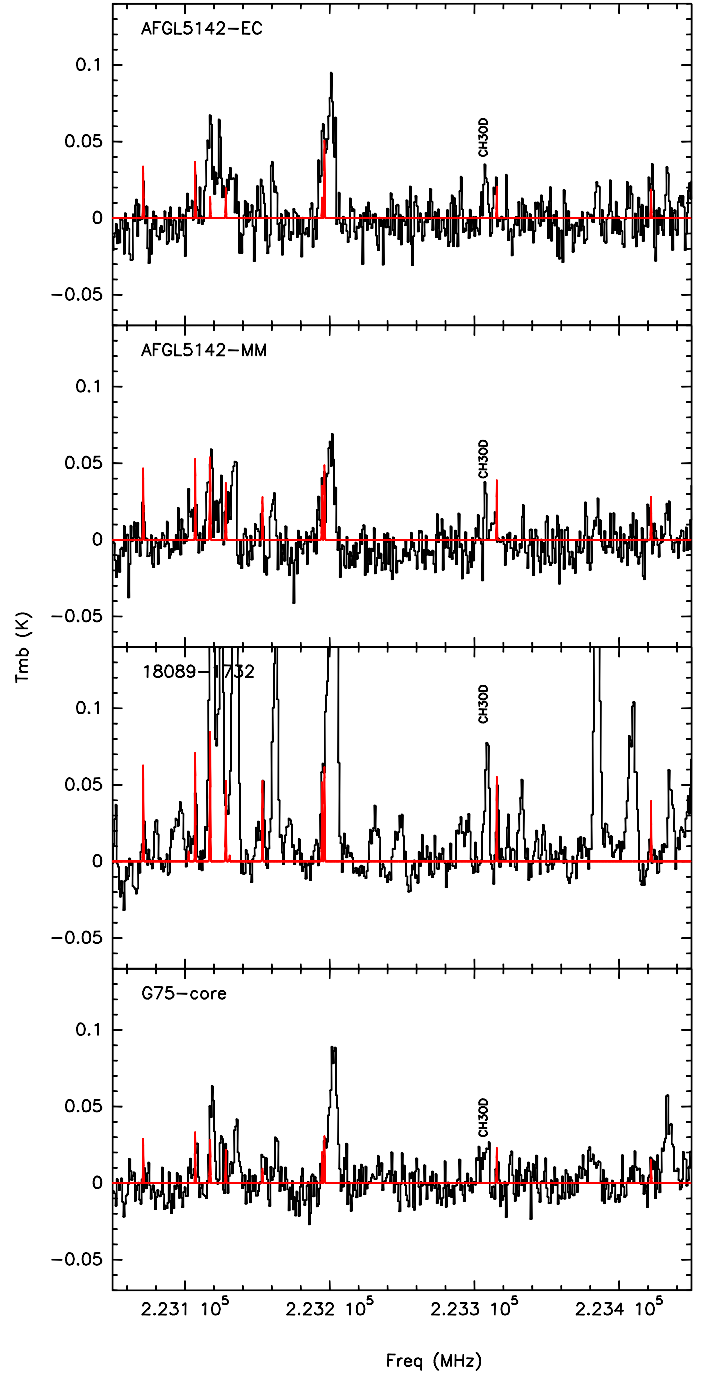


Fig. 1. Example of spectra observed at 1 mm with the CH_2DOH synthetic spectra (red line) used for the identification of the deuterated methanol lines superimposed on them.

used the rotational temperature listed in Table 8 derived from CH_3OH . Examples of the synthetic spectra of CH_2DOH overplotted on the observed spectra are shown in Fig. 1 (red line indicates the synthetic spectra of CH_2DOH). The figure shows that several transitions are (marginally) detected at 1 mm in each of the four cases shown.

3.2.2. Derivation of molecular column densities and rotation temperatures

From the line parameters in Tables B-1 and B-2, we derived rotation temperature (T_{rot}) and total column densities, N , of CH_3OH , $^{13}\text{CH}_3\text{OH}$ and CH_2DOH from the rotation diagram method. As an example, in Fig. 2 we show the rotation diagrams obtained for 18089–1732. We will include all rotation diagrams in an Appendix on-line. The method has been applied when the number of transitions detected was sufficient to build a "reliable" rotation diagram: for example, we rejected the results obtained from this method for sources in which rotation diagrams provide meaningless negative temperatures, or for objects in which few lines associated with large uncertainties and/or similar energy of the upper levels have been detected. Specifically, for CH_2DOH the rotation diagram method has given acceptable results only for two sources, AFGL5142–MM and 18089–1732. However, because in AFGL5142–MM we have only two lines, and in 18089–1732 the fit results are not very accurate (bottom panel in Fig. 2), the column densities have been derived also from Eq. (A4) of Caselli et al. (2002b), taking the strongest line detected and assuming the gas temperature equal to T_{rot} derived from CH_3OH .

For $^{13}\text{CH}_3\text{OH}$, we have assumed that all transitions are optically thin; for CH_3OH , we have first derived a rough estimate of the opacity by comparing two identical lines (specifically, we compared the $2_{(-1,2)} - 1_{(-1,1)}$ and the $2_{(0,2)} - 1_{(0,1)}$ transitions) of CH_3OH and $^{13}\text{CH}_3\text{OH}$, and assumed an LTE abundance ratio of $[^{12}\text{C}]/[^{13}\text{C}] = 77$ (Wilson & Rood 1994). From this check, we have derived low opacities (values smaller than 1) in all sources, so that we have decided to compute N and T_{rot} assuming optically thin conditions too. As for NH_3 and NH_2D , the source sizes of CH_3OH and CH_2DOH are unknown, but they are expected to be smaller than the beam size and to have a comparable extent, based on observations at high angular resolution in Orion (Peng et al. 2012). Therefore, to take into account the beam dilution, the column densities in the rotation diagrams have been corrected by assuming the same source sizes as in paper I, namely 6.5, 4.1 and 5.5'' for HMSCs, HMPOs, and UC Hfns, assuming that methanol and its deuterated forms trace approximately the same material. This is a reasonable general assumption also from a theoretical point of view if deuterated methanol is formed from methanol through H–D substitution reactions on dust grains. In principle, CH_2DOH could be formed following other pathways, but the H–D substitution reaction on solid ices remains the most efficient one (Nagaoka et al. 2005). Moreover, due to the lack of direct measurements in the cores, assuming a different source size for methanol and their deuterated forms would be an arbitrary choice not supported by observations.

For the deuterated species for which only one line is detected, and for sources in which $N(^{13}\text{CH}_3\text{OH})$ cannot be derived from rotation diagrams, we derived N using Eq. (A4) of Caselli et al. (2002b) from one transition only assuming optically thin conditions and adopting as excitation temperature the rotation temperature derived from CH_3OH , available in all sources. The partition functions of all species have been calculated from the approximated expressions valid for asymmetric rotors provided, e.g., in Ratajczak et al. (2011, see also Parise 2004). The results of this analysis are presented in Table 8.

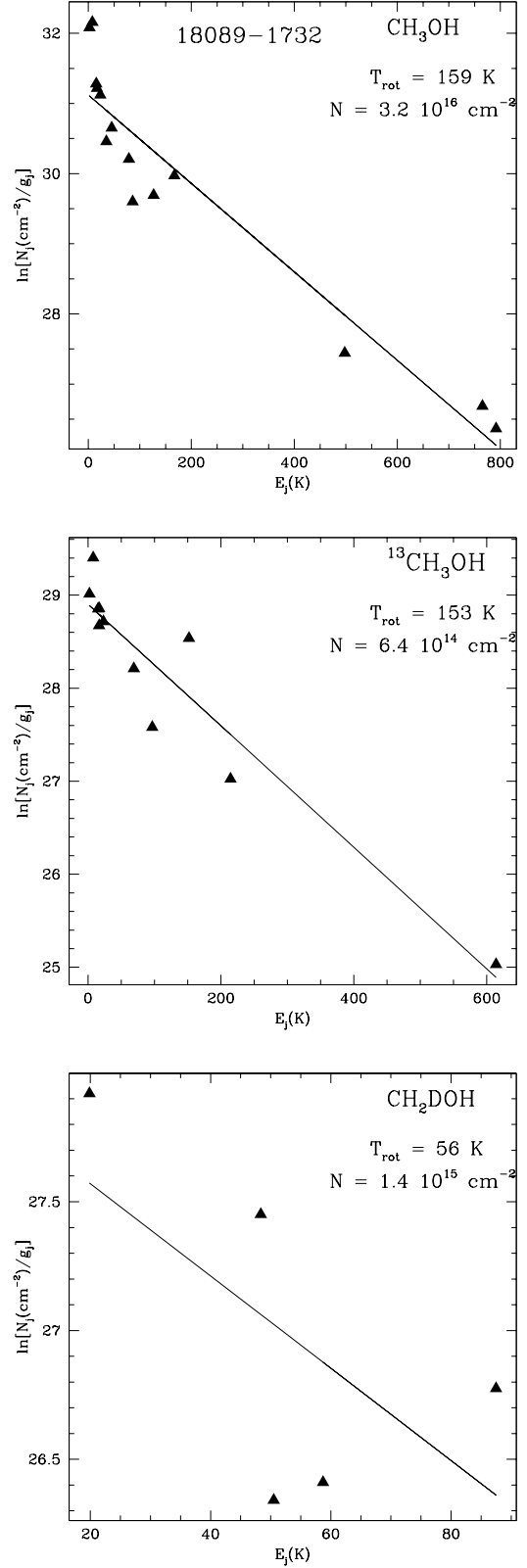


Fig. 2. Rotation diagrams obtained for 18089–1732 from lines of CH_3OH , $^{13}\text{CH}_3\text{OH}$ and CH_2DOH (from top to bottom). Derived rotation temperatures and total column densities are shown in the top-right corner of each panel.

Table 6. Integrated area of the *ortho*- and *para*- lines (Cols. 1 and 2, respectively), and their ratio (Col. 3). Note that the integrated area of the *ortho*- line is equal to the integrated area of the best-fit Gaussian (Table 5) within the errors).

	$\int T_{\text{MB}} dv [o]$ (K km s ⁻¹)	$\int T_{\text{MB}} dv [p]$ (K km s ⁻¹)	$\frac{\int T_{\text{MB}} dv [o]}{\int T_{\text{MB}} dv [p]}$
HMSC			
I00117-MM2	0.66(0.03)	0.16(0.03)	4.1(0.9)
AFGL5142-EC	2.03(0.04)	0.69(0.03)	2.9(0.2)
05358-mm3	0.83(0.04)	0.33(0.03)	2.5(0.3)
G034-G2(MM2)	0.48(0.02)		
G034-F2(MM7)	0.55(0.03)		
G034-F1(MM8)	0.34(0.04)		
G028-C1(MM9)	0.74(0.02)	0.28(0.03)	2.6(0.4)
G028-C3(MM11)	0.12(0.02)		
I20293-WC	2.77(0.03)	1.15(0.03)	2.4(0.1)
I22134-G	0.18(0.02)		
I22134-B	0.20(0.02)	0.13(0.02)	1.5(0.4)
HMPO			
I00117-MM1	0.38(0.03)		
I04579-VLA1			
AFGL5142-MM	2.25(0.03)	0.75(0.03)	3.0(0.2)
05358-mm1	0.51(0.04)	0.26(0.03)	2.0(0.4)
18089-1732	2.33(0.06)	1.02(0.04)	2.3(0.2)
18517+0437	0.50(0.02)		
G75-core	0.29(0.03)		
I20293-MM1	2.44(0.03)	0.84(0.03)	2.9(0.2)
I21307			
I23385	0.13(0.03)		
UC HII			
G5.89-0.39	0.54(0.03)		
I19035-VLA1	0.62(0.03)		
19410+2336	1.98(0.03)	0.72(0.03)	2.8(0.2)
ON1	1.33(0.03)	0.45(0.03)	3.0(0.3)
I22134-VLA1	0.11(0.02)		
23033+5951	0.88(0.03)	0.36(0.02)	2.4(0.2)
NGC7538-IRS9	0.16(0.03)		

4. Discussion

4.1. The *ortho*-/*para*- ratio of NH₂D

The total column density of NH₂D has been derived from lines of *ortho*-NH₂D taking into account the statistical o/p ratio (3:1). In the sources detected also in the *para*-NH₂D line at ~ 110 GHz (see Fig. A-5), we have verified if the assumption is correct: first, we have fit the hyperfine structure of the *para*-NH₂D line, and found that all detected lines are optically thin. Because most of the *ortho*-NH₂D lines detected are either optically thin or have $\tau \leq 1$, we have decided to compare the integrated areas of the two transitions under the channels with signal. These are reported in Table 6. As we can see, the ratio $\int T_{\text{MB}} dv [o] / \int T_{\text{MB}} dv [p]$ is consistent with 3 within the errors in most of the sources: the mean value is 2.6, with standard deviation 0.6, hence consistent with three.

Shah & Wootten (2001) have found similar results in a sample of protostellar cores, in which they compare the integrated intensity of the same two transitions, and derived a mean value of the o/p ratio of 3.2 (with a larger standard deviation of ~ 1.3). Comparable values have been also found by Pillai et al. (2007) in infrared dark clouds and by Tiné et al. (2000) in the two dark molecular clouds L134N and TMC1.

4.2. On the NH₃ and NH₂D excitation temperatures

The excitation temperatures of the three lines examined in the previous sections have very similar mean values: 7.8, 8.2 and 7.5 K for NH₃(1,1), NH₃(2,2) and *ortho*-NH₂D, respectively. The NH₃(1,1) and (2,2) lines are also well correlated (see upper panel of Fig. 3), while the excitation temperatures of the *ortho*-NH₂D line and that of NH₃(1,1) are not correlated due to the different dispersion around the average values: in fact, T_{ex} of NH₃(1,1) spans a range from ~ 3.5 K to 15 K, while T_{ex} of the *ortho*-NH₂D lines is distributed tightly around the average value. This may indicate either that *ortho*-NH₂D is in sub-thermal conditions, as it was suggested by the asymmetric pattern of the hyperfine structure observed in some spectra (see Sect. 3.1.1), or to the fact that we are neglecting the correction for beam dilution. The former hypothesis seems plausible for the *ortho*-NH₂D line, which has a high critical density (~ 10⁶ cm⁻³). About the possible different beam dilution: as stated in Sect. 3.1.3, in the few cores in which both NH₃ (1,1) and *ortho*-NH₂D(1_{-1,1} – 1_{0,1}) have been mapped at high angular resolution, the emissions have comparable extension, despite the different critical densities. Therefore, sub-thermal conditions of the *ortho*-NH₂D lines seem the most likely explanation to the different excitation temperatures.

4.3. Deuterated fraction of NH₃

By dividing $N(\text{NH}_2\text{D})$ for $N(\text{NH}_3)$ we have computed $D_{\text{frac}}(\text{NH}_3)$. The three parameters are given in Table 7. The average values of $D_{\text{frac}}(\text{NH}_3)$ for HMSCs, HMPOs and UC HII, are 0.26 (0.23 if one excludes the “warm” HMSCs, see Sect. 2), 0.34 and 0.21 respectively. These values are consistent with those obtained by Pillai et al. (2007) in a sample of infrared-dark clouds, for which, however, the evolutionary stage of the embedded sources was not determined. The mean $D_{\text{frac}}(\text{NH}_3)$ is thus maximum at the HMPO stage, although the large dispersion of the data does not allow to find a statistical difference between the three groups. This is apparent in Fig. 4, where we compare the total column densities of NH₂D and NH₃: the plot shows that the three groups are not clearly separated. Kolmogorov-Smirnov tests applied to the data confirm that the difference is not statistically significant. If one compares Fig. 4 with the same plot made in paper I for N₂H⁺, we note clearly that, unlike $D_{\text{frac}}(\text{N}_2\text{H}^+)$, $D_{\text{frac}}(\text{NH}_3)$ does not decrease with core evolution. Thus, it is not a tracer of pre-protostellar or young protostellar objects, because it keeps above 0.1 even in the evolved stage of UC HII region. Moreover, because for both N₂H⁺ and NH₃ the deuteration in the gas-phase is linked to H₂D⁺, our results would confirm that the formation of NH₂D is largely influenced by surface chemistry.

Furthermore, $D_{\text{frac}}(\text{NH}_3)$ does not show any clear anti-correlation with typical indicators of evolution. This is suggested by Figs. 5 and 6, where we plot $D_{\text{frac}}(\text{NH}_3)$ against the gas temperature and the line widths of the (1,1) transition, both known to increase with time (e.g., Sánchez-Monge et al. 2013): by applying statistical tests, we even find that $D_{\text{frac}}(\text{NH}_3)$ could be slightly correlated with both the ammonia rotation temperature (Pearson’s linear correlation coefficient $\rho \sim 0.2$) and line widths (Pearson’s linear correlation coefficient $\rho \sim 0.4$). On the contrary, $D_{\text{frac}}(\text{N}_2\text{H}^+)$ is anti-correlated with both parameters, as shown in Fig. 2 of paper I. We stress, however, that the p -value (measure of the probability of chance correlation) is 0.12 for $D_{\text{frac}}(\text{NH}_3)$ vs T_{rot} , and 0.22 for $D_{\text{frac}}(\text{NH}_3)$ vs $\Delta v(1,1)$. Therefore, because typically the significance level under which

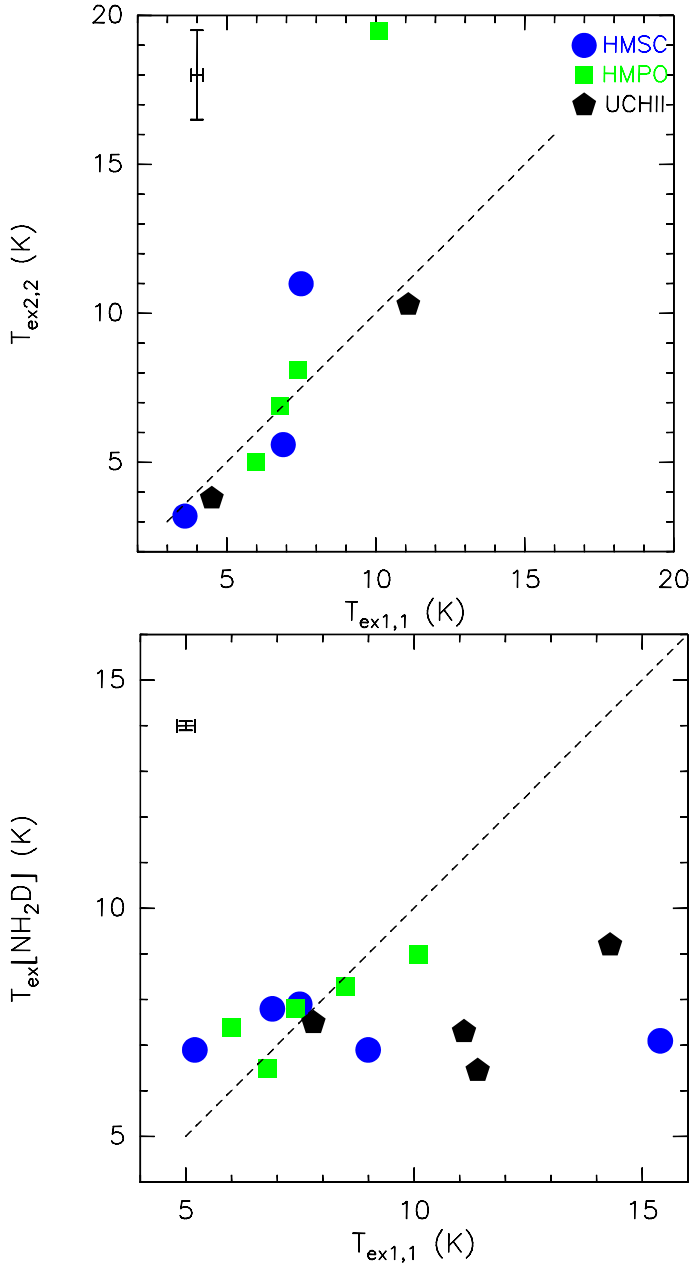


Fig. 3. Comparison between the excitation temperatures of $\text{NH}_3(1,1)$, $T_{\text{ex}1,1}$, and both $T_{\text{ex}2,2}$ (upper panel) and T_{ex} of the *ortho*- NH_2D line (lower panel). In both panels, blue circles correspond to HMSCs, green squares show HMPOs, and black pentagons correspond to UC HII regions, and the dashed line indicates $y = x$. Typical error bars are indicated in the top-left corner of each panel.

one can reject the null hypothesis is $p \sim 0.1$, both correlations are very weak from a statistical point of view. Nevertheless, the relevant result provided by Figs. 5 and 6 is the absence of anti-correlation, contrary to what found for $D_{\text{frac}}(\text{N}_2\text{H}^+)$.

4.4. Deuterated fraction of methanol

In the six objects detected in CH_2DOH , we have computed $D_{\text{frac}}(\text{CH}_3\text{OH}) = N(\text{CH}_2\text{DOH})/N(\text{CH}_3\text{OH})$. The results are listed

Table 7. Rotation temperatures, total column densities of NH_3 and NH_2D , and ammonia deuterated fraction derived as explained in Sect. 3.1.

source	T_{rot} (K)	N_{NH_3} ($\times 10^{14} \text{ cm}^{-2}$)	$N_{\text{NH}_2\text{D}}$ ($\times 10^{14} \text{ cm}^{-2}$)	$D_{\text{frac}}(\text{NH}_3)$
HMSCs				
I00117-MM2	17.9(0.6)	4.22(0.06)	2.62(0.05)	0.62(0.02)
AFGL5142-EC	20(1)	10.39(0.03)	4.31(0.07)	0.41(0.01)
05358-mm3	21.1(0.3)	9.27(0.02)	4.62(0.07)	0.498(0.008)
G034-G2	15.2(0.4)	12.12(0.04)	2.40(0.02)	0.198(0.002)
G034-F2	— ^a	— ^a	2.1(0.02)	—
G034-F1	— ^a	— ^a	0.12(0.02)	—
G028-C1	17.7(0.3)	20.70(0.02)	0.47(0.03)	0.023(0.002)
G028-C3	11.7(0.4)	8.29(0.04)	0.07(0.02)	0.009(0.004)
I20293-WC	19.4(0.4)	13.96(0.02)	0.78(0.02)	0.519(0.002)
I22134-G	18.2(0.4)	2.98(0.06)	0.12(0.03)	0.04(0.01)
I22134-B	14.9(0.5)	2.76(0.06)	0.16(0.01)	0.057(0.005)
HMPOs				
I00117-MM1	16.4(0.7)	2.05(0.05)	0.24(0.04)	0.12(0.02)
I04579-VLA1	20(2)	0.56(0.03)	≤ 0.06	≤ 0.1
AFGL5142-MM	21.5(0.5)	10.65(0.02)	5.50(0.08)	0.516(0.008)
05358-mm1	21.6(0.3)	8.53(0.03)	1.63(0.07)	0.191(0.008)
18089-1732	28(1)	35.55(0.02)	9.1(0.1)	0.255(0.003)
18517+0437	22(1)	5.32(0.05)	7.3(0.1)	1.37(0.03)
G75-core	26.9(0.6)	8.94(0.07)	0.19(0.04)	0.022(0.005)
I20293-MM1	17(1)	15.82(0.03)	3.07(0.02)	0.194(0.002)
I21307	20(1)	2.99(0.05)	≤ 0.05	≤ 0.02
I23385	23(1)	2.53(0.05)	0.09(0.03)	0.04(0.01)
UC HII				
G5.89-0.39	29.0(0.3)	17.06(0.04)	12.0(0.5)	0.71(0.03)
I19035-VLA1	24(1)	12.67(0.05)	0.40(0.04)	0.031(0.003)
19410+2336	18.7(0.2)	13.47(0.05)	2.2(0.03)	0.165(0.002)
ON1	21.4(0.7)	36.58(0.03)	4.57(0.08)	0.125(0.002)
I22134-VLA1	— ^a	— ^a	0.08(0.02)	—
23033+5951	16.4(0.2)	10.10(0.07)	2.37(0.07)	0.234(0.009)
NGC7538-IRS9	20.4(0.2)	7.23(0.06)	0.10(0.04)	0.014(0.005)

Notes. ^(a) Not observed.

in the last column of Table 8. The average $D_{\text{frac}}(\text{CH}_3\text{OH})$ in the three HMPOs detected is ~ 0.04 if one uses $N(\text{CH}_2\text{DOH})$ derived from rotation diagrams, ~ 0.01 if we use the simplified approach from one line only (see Sect. 3.2.2). In the two “warm” HMSCs is ~ 0.0025 . G034-G2 is the unique quiescent HMSC detected in CH_2DOH , and in this core $D_{\text{frac}}(\text{CH}_3\text{OH})$ is ~ 0.015 . For the cores undetected in CH_2DOH , the large majority of the targets observed, we have estimated upper limits of $D_{\text{frac}}(\text{CH}_3\text{OH})$ in this way: we have computed the 3σ level in the spectrum of the $(2_{0,2} - 1_{0,1})e0$ line, which is the transition with the smallest energy of the upper level ($E_u \sim 6.5$ K) at 3 mm, and estimated the upper limit to the integrated area from the relation $\int T_{\text{MB}} dv = 3\sigma \frac{\Delta V}{2\sqrt{\ln 2/\pi}}$, valid for a Gaussian line having peak temperature = 3σ . We have assumed $\Delta V = 1 \text{ km s}^{-1}$, which is the average value of the detected CH_2DOH lines both in the HMSCs and the HMPOs (see Table B-1); then, the upper limit on the CH_2DOH column density has been computed using the same equations as for the detected sources. We have followed the same method to compute the upper limits on the $^{13}\text{CH}_3\text{OH}$ lines, using this time the $(2_{0,2} - 1_{0,1} + +)$ line.

The case of the HMSC G034-G2 is quite peculiar, because it is the only quiescent starless core detected in CH_2DOH (in one line only), and its $D_{\text{frac}}(\text{CH}_3\text{OH})$ exceeds 0.01, while the upper limits found in the other quiescent HMSCs are lower. Its detection is thus quite doubtful. We have checked for possible contamination from other species by running synthetic spectra (see Sect. 3.2.1) of molecules that possess transitions at a similar frequency, and concluded that indeed contributions from lines of CH_3OOH , and HCCCH_2OH are possible. Therefore, this detection remains doubtful.

Although the number of detections is low, and the results are affected by the faintness of the CH_2DOH lines, these findings suggest that high values of $D_{\text{frac}}(\text{CH}_3\text{OH})$ tend to be associated with “warm” HMSCs and HMPOs rather than with cores very young (quiescent HMSCs) or evolved (UC Hns), although the remarkable value derived in G034–G2 (if confirmed) suggests that the story could not be so simple. Parise et al. (2006) measured values of $D_{\text{frac}}(\text{CH}_3\text{OH})$ higher than ours by at least an order of magnitude in a sample of low-mass protostellar cores. Nevertheless, due to the smaller linear resolution of their observations (most of their cores are in Perseus, at a distance of ~ 200 pc), their measurements should be less affected than ours by non-deuterated gas along the line of sight. Moreover, our $D_{\text{frac}}(\text{CH}_3\text{OH})$ are consistent with the upper limits found by Loinard et al. (2003) in high-mass protostellar objects (where, however, they observed D_2CO and derived $[\text{D}_2\text{CO}] / [\text{H}_2\text{CO}] < 0.5\%$), as well as with observations of deuterated methanol in the intermediate-mass protostar NGC7129-FIRS2 (Fuente et al. 2014) and in Orion BN/KL (Peng et al. 2012).

4.5. Deuteration and core evolution: the role of surface chemistry

In Fig. 7 we report the mean values of D_{frac} obtained in HMSCs, HMPOs and UC Hns for the four molecular species investigated so far towards our source sample: N_2H^+ (paperI), HNC (paperII), NH_3 and CH_3OH (this work). We show separately the values derived for quiescent HMSCs and “warm” HMSCs to underline the effect of nearby star formation. We also include the mean values (with standard deviation) of the ammonia rotation temperatures derived in this work to highlight possible (anti-)correlation between D_{frac} and gas temperature. Inspection of Fig. 7 leads to these immediate results: (i) only $D_{\text{frac}}(\text{N}_2\text{H}^+)$ shows a net decrease from the HMSC stage to the HMPO stage, associated to a temperature enhancement; (ii) $D_{\text{frac}}(\text{NH}_3)$ remains nearly constant in all stages; (iii) $D_{\text{frac}}(\text{CH}_3\text{OH})$ is maximum in the HMPO stage, although this result must be interpreted carefully due to the low number of detections and the caveats on the methods to derive D_{frac} (see Sects. 3.2.2); (iv) the behaviour of $D_{\text{frac}}(\text{HNC})$ is something in between that of $D_{\text{frac}}(\text{N}_2\text{H}^+)$ and that of $D_{\text{frac}}(\text{NH}_3)$, because its maximum value is found in the HMSC phase, like $D_{\text{frac}}(\text{N}_2\text{H}^+)$, but the statistically significant decrease when going to the HMPO stage is not seen. In paperII we have already discussed this difference, and attributed it to a slower process of destruction of DNC into the warm gas with respect to N_2D^+ .

As stated in Sect. 1, $D_{\text{frac}}(\text{N}_2\text{H}^+)$ and $D_{\text{frac}}(\text{CH}_3\text{OH})$ should represent the two “extreme” situations under which deuteration can occur: in the gas only and on grain mantles only, respectively. In the classical framework, both ammonia and methanol (and their deuterated isotopologues) are produced efficiently on grain mantles during the pre-stellar phase through hydrogenation of N and CO, respectively. Specifically, hydrogenation of CO forms sequentially formaldehyde first and then methanol: thus, as time proceeds, the formation of methanol and their deuterated isotopologues is boosted, until the energy released by the nascent protostellar object in the form of radiation increases the temperature of its environment, causing the evaporation of the grain mantles and the release of these molecules into the gas. As the temperature increases and the protostar evolves towards the UC Hn region phase, the deuterated species are expected to be gradually destroyed due to the higher efficiency of the backward endothermic reactions (see Caselli & Ceccarelli 2012 for a review). The trends shown in Fig. 7 are consistent with this

classic framework, and show clearly that high deuterated fractions of ammonia cannot be used as evolutionary indicator of a high-mass star forming core. On the other hand, $D_{\text{frac}}(\text{CH}_3\text{OH})$ may be potentially a tracer of the very early stages of the protostellar evolution, at which the evaporation/sputtering of the grain mantles is most efficient. Our results, however, suffers from a too low statistics, and needs to be reinforced by other observations of deuterated methanol at higher sensitivity.

Chemical models of low-mass star-forming cores predict how the abundance of several deuterated species varies during the evolution, including the amount formed on ices during the early cold phase (e.g. Taquet et al. 2012, Aikawa et al. 2012). Aikawa et al. (2012) show that the relative abundance ratios $[\text{NH}_2\text{D}]/[\text{NH}_3]$ and $[\text{CH}_2\text{DOH}]/[\text{CH}_3\text{OH}]$ in the ices during the pre-stellar phase are both in between 0.01 and 0.1. These values are consistent with $D_{\text{frac}}(\text{CH}_3\text{OH})$ measured in this work, and confirm that methanol and its deuterated forms are products of the evaporation of grain mantles. On the other hand, $D_{\text{frac}}(\text{NH}_3)$ measured in our work (≥ 0.1) is larger than the values predicted on ices by Aikawa et al. (2012), suggesting that the emission we see must include a contribution from material formed through gas-phase reactions. Awad et al. (2014) modeled the deuterium chemistry of star-forming cores using both gas-phase and grain-surface reactions, but focus on the protostellar phase, when the evaporation of the icy mantles of dust grains is maximum. The model that best reproduces a HMPO predicts $D_{\text{frac}}(\text{NH}_3) \sim 10^{-3} - 10^{-2}$ and $D_{\text{frac}}(\text{CH}_3\text{OH}) \leq 4 \times 10^{-3}$, both smaller than our observed values. However, the abundance of deuterated species strongly depends on the density of the gas: lower-density cores have lower abundances of deuterated species, due to a smaller degree of CO depletion. Therefore, larger core densities could be able to reproduce the larger deuterated fractions that we measure.

In any case, the huge dispersion of the data do not allow us to derive firmer quantitative conclusions, and push us to interpret any comparison with chemical models with caution. Moreover, the chemical models of Taquet et al. (2012) and Aikawa et al. (2012) neglect the spin states of the deuterated species, which can significantly influence the deuterium fractionation depending on the ortho-to-para H_2 ratio (Flower et al. 2006). Nevertheless, the clear different trend between $D_{\text{frac}}(\text{NH}_3)$ and $D_{\text{frac}}(\text{N}_2\text{H}^+)$ indicates undoubtedly that gas-phase chemistry cannot play a dominant role in the production of NH_2D .

5. Summary and conclusions

The deuterated fraction of species that can be formed on dust grains (in part, like NH_3 , or uniquely, like CH_3OH) has been investigated towards a sample of dense cores harbouring different evolutionary stages of the high-mass star formation process. As expected, the deuterated fraction of these species and those of molecules totally or predominantly formed in the gas, like N_2H^+ and HNC, evolve differently with time and with temperature: $D_{\text{frac}}(\text{NH}_3)$ does not show statistically significant changes with evolution, unlike $D_{\text{frac}}(\text{N}_2\text{H}^+)$ and $D_{\text{frac}}(\text{HNC})$, which decrease (especially $D_{\text{frac}}(\text{N}_2\text{H}^+)$) when temperature increases. Few lines of CH_2DOH and CH_3OD are clearly detected, and only towards protostellar cores or externally heated starless cores. Only one line of CH_2DOH could have been detected in a quiescent starless core, but the detection is doubtful. No lines of deuterated methanol species are detected in UC Hn regions. This work clearly supports the scenario in which the contribution of surface chemistry to the formation of deuterated forms of ammonia

Table 8. Rotation temperatures and total column densities for CH₃OH, ¹³CH₃OH and CH₂DOH derived from rotation diagrams, unless when specified differently. For CH₂DOH, in the sources where only one line has been detected, we have computed the total column density from Eq. (A4) of Caselli et al. (2002b), assuming the temperatures obtained from CH₃OH.

source	CH ₃ OH		¹³ CH ₃ OH		CH ₂ DOH		<i>D</i> _{frac} (CH ₃ OH)
	<i>T</i> _{rot} K	<i>N</i> (×10 ¹⁴)cm ⁻²	<i>T</i> _{rot} K	<i>N</i> (×10 ¹³)cm ⁻²	<i>T</i> _{rot} K	<i>N</i> (×10 ¹⁴)cm ⁻²	
HMSC							
I00117–MM2	19.0	1.80		≤ 0.3		≤ 0.013	≤ 0.007
AFGL5142–EC	41.5	61.5	14.1	5.27	– ^{<i>a</i>}	0.11 ^{<i>a</i>}	0.002(0.001)
05358–mm3	26.1	24.9	5.1	1.53		0.08	0.003(0.001)
G034–G2(MM2)	6.0	1.75	– ^{<i>a</i>}	0.09 ^{<i>a</i>}		0.03	0.015(0.07)
G034–F2(MM7)	5.7	0.95		≤ 0.15		≤ 0.007	≤ 0.007
G034–F1(MM8)	17.5	2.24		≤ 0.3		≤ 0.01	≤ 0.006
G028–C1(MM9)	14.2	2.69	6.8	0.71		≤ 0.01	≤ 0.004
I20293–WC	24.4	3.44		≤ 0.5		≤ 0.02	≤ 0.005
I22134–G	18.1	2.87		≤ 0.3		≤ 0.01	≤ 0.004
I22134–B	7.8	0.35		≤ 0.2		≤ 0.007	≤ 0.02
HMPO							
I00117–MM1	27.7	1.22		≤ 0.6		≤ 0.02	≤ 0.02
AFGL5142–MM	112.6	262.7	7.9	5.81	10.4	19.0 ^{<i>b</i>} ; 2.1 ^{<i>c</i>}	0.07(0.03) ^{<i>b</i>} ; 0.008(0.004) ^{<i>c</i>}
05358–mm1	84.0	125.1	– ^{<i>a</i>}	6.1 ^{<i>a</i>}		≤ 0.13	≤ 0.001
18089–1732	158.6	318.1	153.0	64.2	56	14.0 ^{<i>b</i>} ; 4.0 ^{<i>c</i>}	0.04(0.02) ^{<i>b</i>} ; 0.01(0.01) ^{<i>c</i>}
18517+0437	137.6	209.2	44.5	25.6		≤ 0.2	≤ 0.001
G75–core	108.5	150.6	– ^{<i>a</i>}	4.2 ^{<i>a</i>}		0.55	0.005(0.003)
I20293–MM1	35.1	27.5	– ^{<i>a</i>}	0.9 ^{<i>a</i>}		≤ 0.04	≤ 0.001
I21307	29.4	6.54		≤ 0.5		≤ 0.03	≤ 0.004
I23385	25.3	18.0	– ^{<i>a</i>}	0.3 ^{<i>a</i>}		≤ 0.02	≤ 0.01
UC H _{II}							
G5.89–0.39	64.1	128.1	37.9	14.0		≤ 0.14	≤ 0.001
I19035–VLA1	30.7	16.4	28.6	4.80		≤ 0.03	≤ 0.002
19410+2336	31.1	20.2	20.8	5.79		≤ 0.03	≤ 0.001
ON1	31.3	32.4	25.5	8.98		≤ 0.02	≤ 0.0007
I22134–VLA1	19.4	1.64		≤ 0.3		≤ 0.02	≤ 0.009
23033+5951	24.2	12.0	37.4	8.33		≤ 0.02	≤ 0.002
NGC7538–IRS9	28.7	17.6	– ^{<i>a</i>}	0.5 ^{<i>a</i>}		≤ 0.02	≤ 0.001

Notes. ^(a) Only lines with very close upper energies are detected, and the rotation diagram provides a meaningless negative T_{rot} . Therefore, the column density has been derived from the transition ($2_{0,2} - 1_{0,1}$)++ assuming LTE conditions and T_{rot} from methanol; ^(b) derived from rotation diagrams; ^(c) derived from the transition ($5_{2,3} - 4_{1,4}$)e1 assuming LTE conditions and T_{rot} from methanol.

is relevant, and hence that $D_{\text{frac}}(\text{N}_2\text{H}^+)$ remains the best indicator of massive starless cores. High values of $D_{\text{frac}}(\text{CH}_3\text{OH})$ seem suitable to trace the earliest protostellar phases, at which the evaporation/sputtering of the grain mantles is most efficient, but this result needs to be supported by further, higher sensitivity observations. The data presented in this work represent an excellent starting point for higher angular resolution studies to address further questions. In particular: if the various deuterated molecules are formed with different mechanisms, do we expect a different distribution of the emission too?

Acknowledgments. FF and AP are grateful to the IRAM-30m staff for their help in the observations at the IRAM-30m telescope. GB is grateful to Amanda Kepley for her help during the GBT observations, and to Jeff Magnum for providing the procedures to convert the GBT spectra from GBTIDL to CLASS format. AP acknowledges the financial support from UNAM, and CONACyT, México. GB is supported by the Spanish MICINN grant AYA2008-06189-C03-01 (co-funded with FEDER funds) and by the Italian Space Agency (ASI) fellowship under contract number I/005/07/01. PC acknowledges the financial support of the European Research

Council (ERC; project PALs 320620). AS-M is supported by the Deutsche Forschungsgemeinschaft (DFG) through the collaborative research grant SFB 956 "Conditions and Impact of Star Formation", project area A6. The research leading to these results has received funding from the European Commission Seventh Framework Programme (FP/2007-2013) under grant agreement N 283393 (RadioNet3).

References

- Anglada, G., Estalella, R., Mauersberger, R., Torrelles, J.M., Rodriguez, L.F. et al. 1995, *ApJ*, 443, 682
- Aikawa, Y., Herbst, E., Roberts, H., Caselli, P. 2005, *ApJ*, 620, 330
- Aikawa, Y., Wakelam, V., Hersant, F., Garrod, R.T., Herbst, E. 2012, *ApJ*, 760, 40
- Awad, Z., Viti, S., Bayet, E., Caselli, P. 2014, *MNRAS*, 443, 275
- Beuther, H., Churchwell, E.B., McKee, C.F., Tan, J.C. 2007, *PPV*, B. Reipurth, D. Jewitt, and K. Keil (eds.), University of Arizona Press, Tucson, p. 165
- Busquet, G. 2010, PhD Thesis, University of Barcelona
- Busquet, G., Palau, A., Estalella, R. et al. 2010, *A&A*, 517, L6
- Busquet, G., Palau, A., Estalella, R. et al. 2009, *A&A*, 506, 1183
- Butler, M.J. & Tan, J.C. 2009, *ApJ*, 696, 484
- Butler, M.J., Tan, J.C., Kainulainen, J. 2014, *ApJ*, 782, L30
- Caselli, P., Vastel, C., Ceccarelli, C. et al. 2008, *A&A*, 492, 703

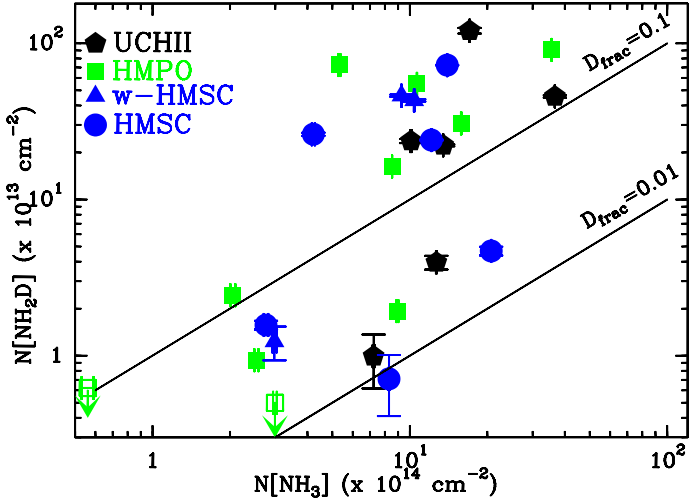


Fig. 4. Comparison between the total column density of NH_2D , $N(\text{NH}_2\text{D})$, and NH_3 , $N(\text{NH}_3)$. Blue symbols correspond to HMSCs (triangles: warm cores, see Sect. 2); green squares show HMPOs (open squares are upper limits); black pentagons correspond to UCHII regions. In most cases, the errorbars are barely visible because comparable to (or smaller than) the size of the symbol. The straight lines represent the loci of $D_{\text{frac}}(\text{NH}_3) = 0.01$ and 0.1 .

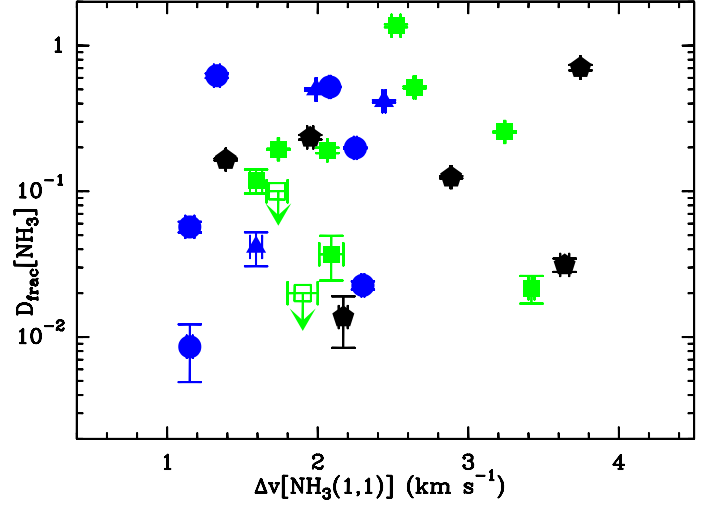


Fig. 6. $D_{\text{frac}}(\text{NH}_3)$ against the $\text{NH}_3(1,1)$ line width. The symbols have the same meaning as in Fig. 4. No clear (anti-)correlation is found between the two parameters, like in Fig. 5. The errorbars are barely visible because comparable to (or smaller than) the size of the symbol.

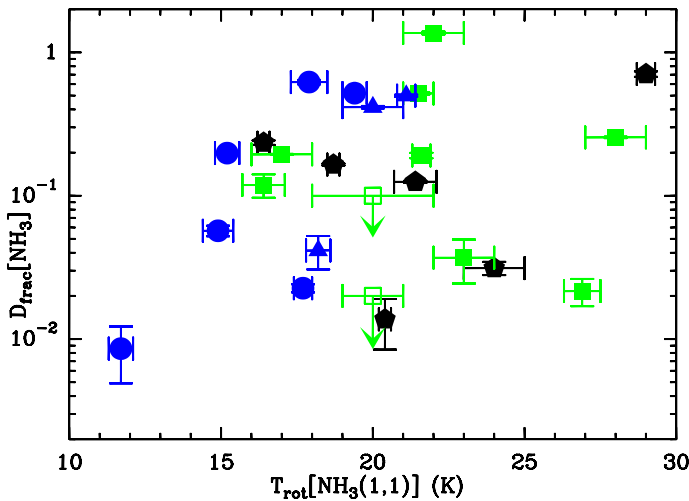


Fig. 5. $D_{\text{frac}}(\text{NH}_3)$ against the ammonia rotation temperature. The symbols have the same meaning as in Fig. 4. No clear (anti-)correlation is found between the two parameters. In some cases, the errorbars are barely visible because comparable to (or smaller than) the size of the symbol.

- Caselli, P. 2002a, P&SS, 50, 1133
 Caselli, P., Walmsley C.M., Zucconi, A. et al. 2002b, ApJ, 565, 344
 Caselli, P. & Ceccarelli, C. 2012, A&ARv, 20, 56
 Crapsi, A., Caselli, P., Walmsley, C.M., et al. 2005, ApJ, 619, 379
 Daniel, F., Faure, A., Wiesenfeld, L., Roueff, E., Lis, D.C., Hily-Blant, P. 2014, MNRAS, 444, 2544
 Emprechtinger, M., Caselli, P., Volgenau, N.H., Stutzki, J., Wiedner, M.C. 2009, A&A, 493, 89
 Flower, D.R., Pineau Des Forêts, G., Walmsley, C.M. 2006, A&A, 449, 621
 Fontani, F., Palau, Aina, Caselli, P. et al. 2011, A&A, 529, L7
 Fontani, F., Caselli, P., Crapsi, A. et al. 2006, A&A, 460, 709
 Fontani, F., Cesaroni, R., Testi, L. et al. 2004, A&A, 414, 299
 Fontani, F., Sakai, T., Furuya, K., Sakai, N., Aikawa, Y., Yamamoto, S. 2014, MNRAS, 440, 448
 Fuente, A., Cernicharo, J., Caselli, P., McCoe, C., Johnstone, D. et al. 2014, A&A, 568, 65
 Garrod, R.T., Wakelam, V., Herbst, E. 2007, A&A, 467, 1103
 Gerlich, D., Herbst, E., Roueff, E. 2002, P&SS, 50, 1275
 Ho, P.T.P. & Townes, C.H. 1983, ARA&A, 21, 239
 Kutner, M.L. & Ulich, B.L. 1981, ApJ, 250, 341
 Leurini, S., Rolfs, R., Thorwirth, S., Parise, B., Schilke, P. et al. 2006, A&A, 454, L47
 Loinard, L., Castets, A., Ceccarelli, C., et al. 2003, SFChem 2002: Chemistry as a Diagnostic of Star Formation, 351
 Miettinen, O., Hennemann, M., Linz, H. 2011, A&A, 534, 134
 Millar, T.J., Bennett, A., Herbst, E. 1989, ApJ, 340, 906
 Müller, H.S.P., Thorwirth, S., Roth, D.A., Winnewisser, G. 2001, A&A, 370, L49
 Müller, H.S.P., Schlöder, F., Stutzki, J., Winnewisser, G. 2005, J. Mol. Struct., 742, 215
 Nagaoka, A., Watanabe, N., Kouchi, A. 2005, ApJ, 624, L29
 Olberg, M., Bester, M., Rau, G., et al. 1985, A&A, 142, L1
 Oliveira, C.M., Hébrard, G., Howk, J.C. et al. 2003, ApJ, 587, 235

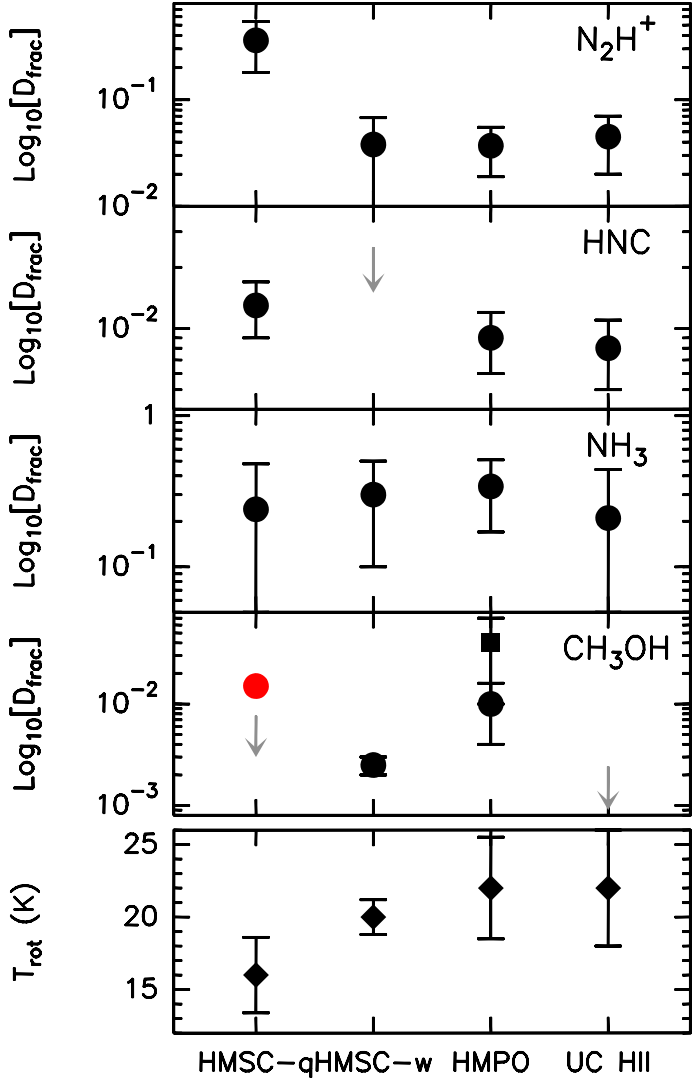


Fig. 7. Panels one to four, from top: comparison between the mean deuterated fractions (black dots) of N_2H^+ (first panel, paperI), HNC (second panel, paperII) NH_3 and CH_3OH (third and fourth panels, this work). The mean values have been computed for each evolutionary group. Quiescent HMSCs (HMSC-q) and warm HMSCs (HMSC-w) have been treated separately. The errorbars indicate the standard deviation. The grey arrows represent mean upper limits for those evolutionary groups in which no sources have been detected. The red dot in the fourth panel represents the doubtful CH_2DOH detection in G034-G2 (see Sect. 4.4), while the square indicates the mean D_{frac} of HMPOs when $N(\text{CH}_2\text{DOH})$ is derived from rotation diagrams for AFGL5142-MM and 18089-732.

Bottom panel: mean rotation temperatures (filled diamonds) derived from ammonia in the four groups (see Table 7).

- Pickett, H.M., Poynter, R.L., Cohen, E.A., Delitsky, M.L., Pearson, J.C., Müller, H.S.P. 1998, JQSRT, 60, 883
- Pillai, T., Kauffmann, J., Wyrowski, F., Hatchell, J., Gibb, A.G., Thompson, M.A. 2011, A&A, 530, 118
- Pillai, T., Wyrowski, F., Hatchell, J., Gibb, A.G., Thompson, M.A. 2007, A&A, 467, 207
- Ratajczak, A., Taquet, V., Kahane, C., Ceccarelli, C., Faure, A., Quirico, E. 2011, 528, L13
- Sánchez-Monge, Á., Palau, Aina, Fontani, F., Busquet, G., Juárez, C., Estalella, R., Tan, J.C., Sepúlveda, I. 2013, MNRAS, 432, 3288
- Sakai, T., Sakai, N., Furuya, K., Aikawa, Y., Hirota, T., Yamamoto, S. 2012, ApJ, 747, 140
- Shah, R.Y. & Wootten, A. 2001, ApJ, 554, 933
- Schöier, F.L., van der Tak, F.F.S., van Dishoeck, E.F., Black, J.H. 2005, A&A, 432, 369
- Tan, J.C., Beltrán, M.T., Caselli, P., Fontani, F., Fuente, A. et al. 2014, arXiv:1402.0919
- Taquet, V., Ceccarelli, C. Kahane, C. 2012, ApJ, 748, L3
- Tiné, S., Roueff, E., Falgarone, E., Gerin, M., Pineau des Forêts, G. 2000, A&A, 356, 1039
- van der Tak, F.F.S., Black, J.H., Schöier, F.L., Jansen, D.J., van Dishoeck, E.F. 2007, A&A, 468, 627
- Wilson, T.L. & Rood, R. 1994, ARA&A, 32, 191

- Palau, Aina, Fuente, A., Girart, J.M., Fontani, F., Boissier, J., et al. 2011, ApJ, 743, L32
- Parise, B., Ceccarelli, C., Tielens, A.G.G.M., Herbst, E., Lefloch, B. et al. 2002, A&A, 393, L49
- Parise, B. 2004, PhD Thesis, Centre d'Etude Spatiale des Rayonnements
- Parise, B., Ceccarelli, C., Tielens, A.G.G.M., Castets, A., Caux, E., Lefloch, B., Maret, S. 2006, A&A, 453, 949
- Peng, T.-C., Despois, D., Brouillet, N., Parise, B., Baudry, A. 2012, A&A, 543, 152

Appendix A: NH_3 and NH_2D spectra

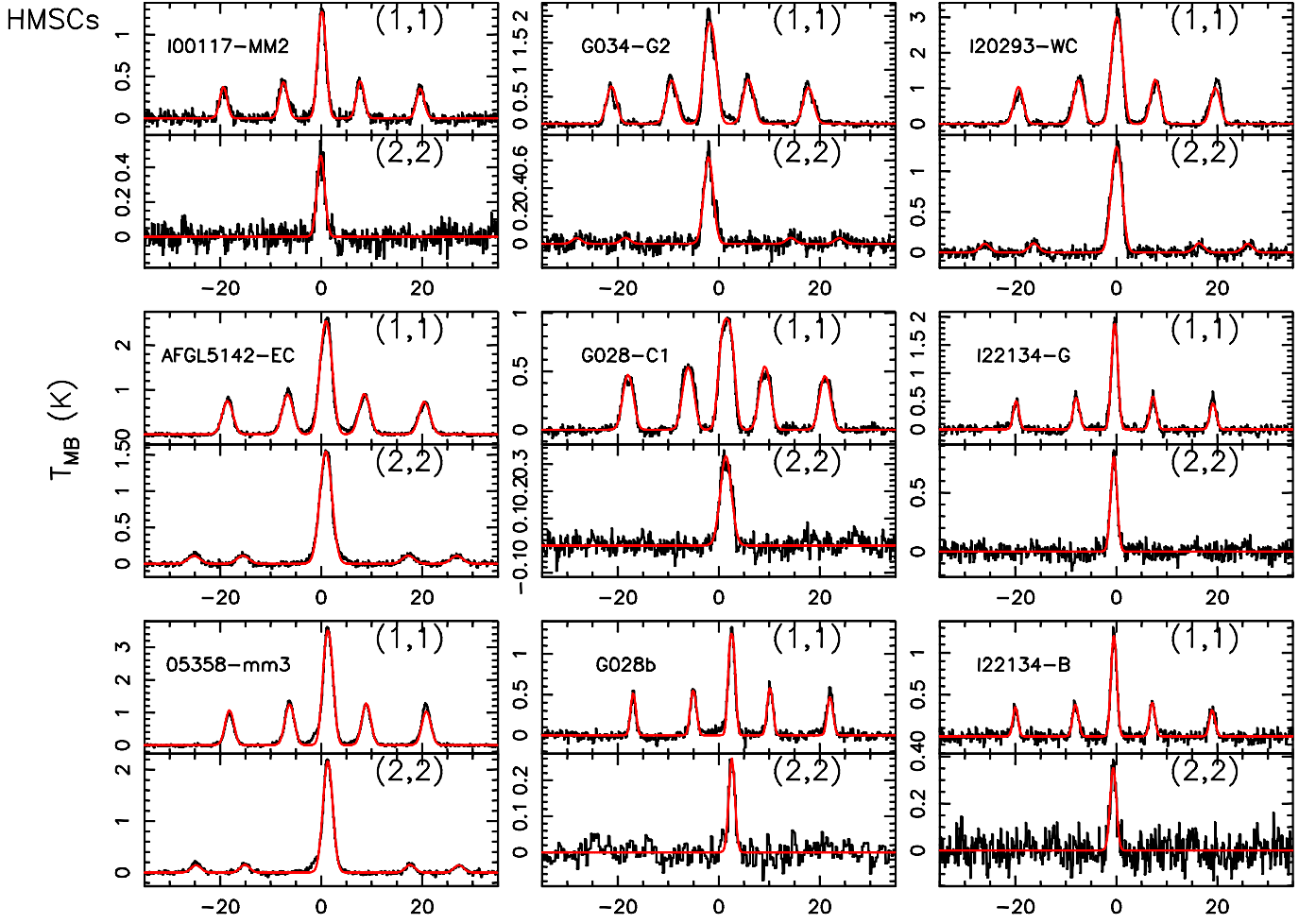


Fig. A-1. GBT spectra of $\text{NH}_3(1,1)$ and $(2,2)$ obtained towards the sources classified as HMSCs. For each spectrum, the x-axis represents a velocity interval of $\pm 35 \text{ km s}^{-1}$ from the systemic velocity listed in Table 1. The y-axis shows the intensity scale in main beam brightness temperature units. In each spectrum, the red curve indicates the best fit either obtained by fitting the hyperfine structure, when possible, or with a single Gaussian (see Sect. 3.1).

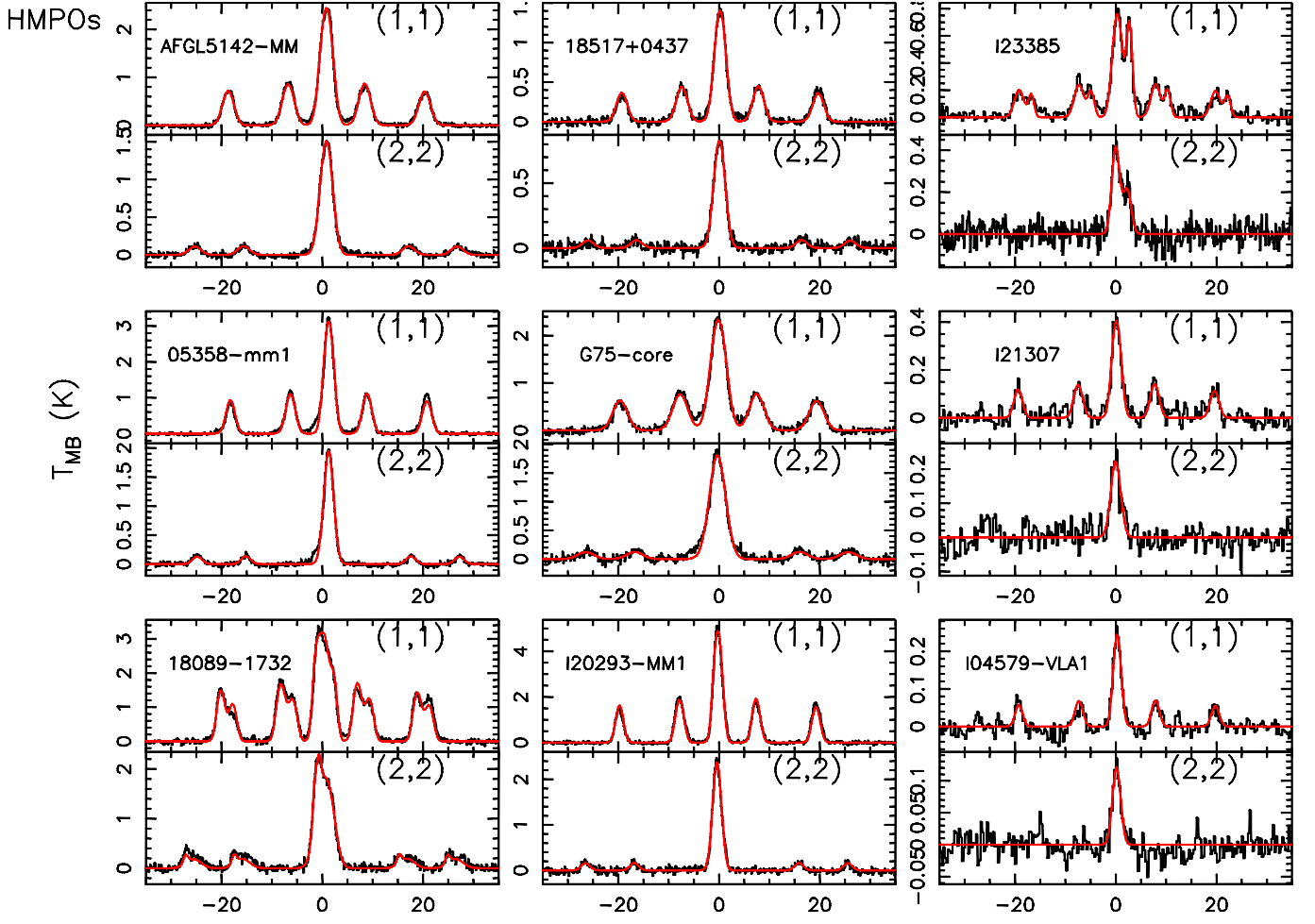


Fig. A-2. Same as Fig. A-1 for the sources classified as HMPOs. Note that for the spectra of I23385 and 18089-1732, a fit with two velocity components has been performed.

UCHIIs

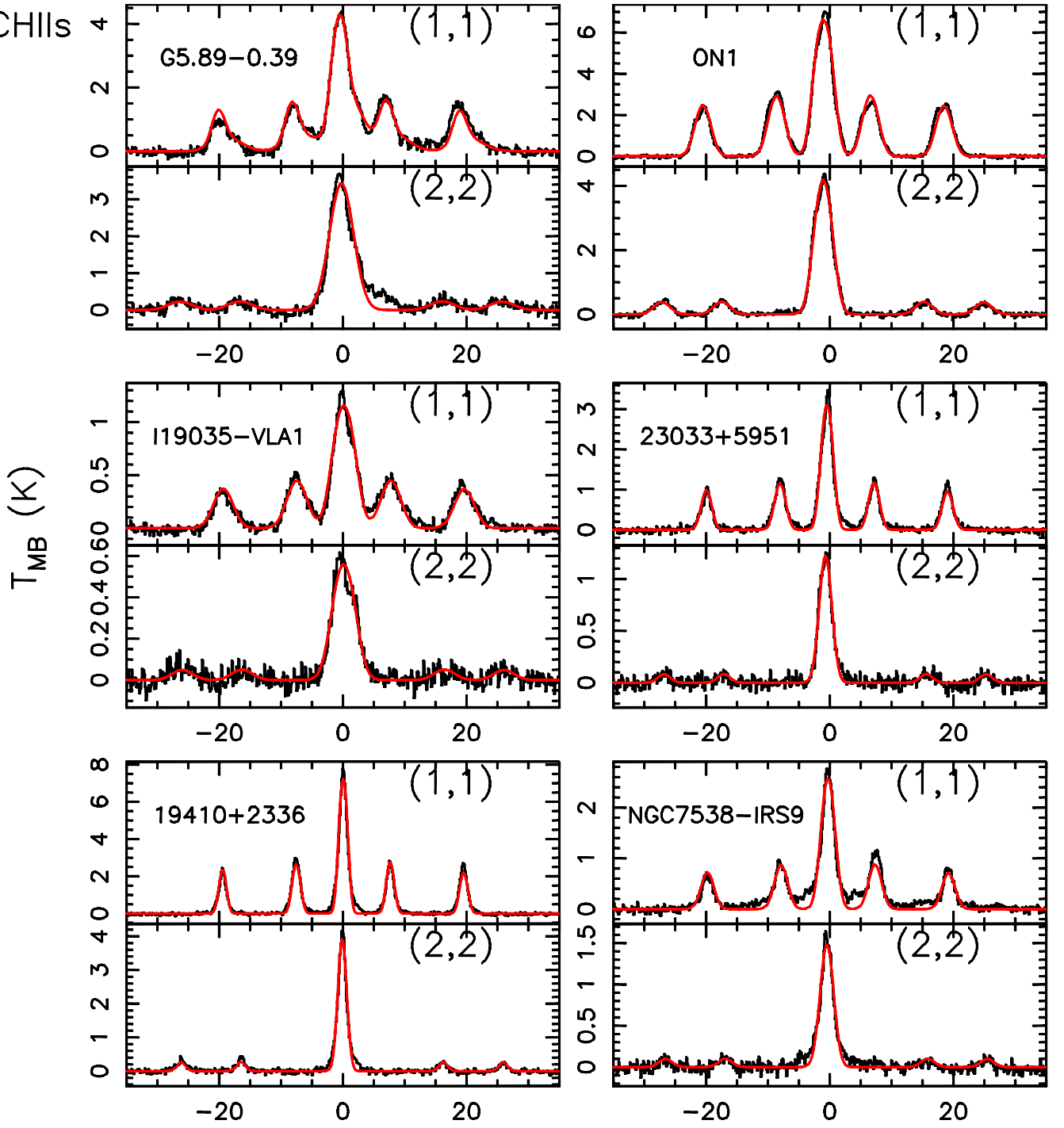


Fig. A-3. Same as Fig. A-1 for the sources classified as UC HII.

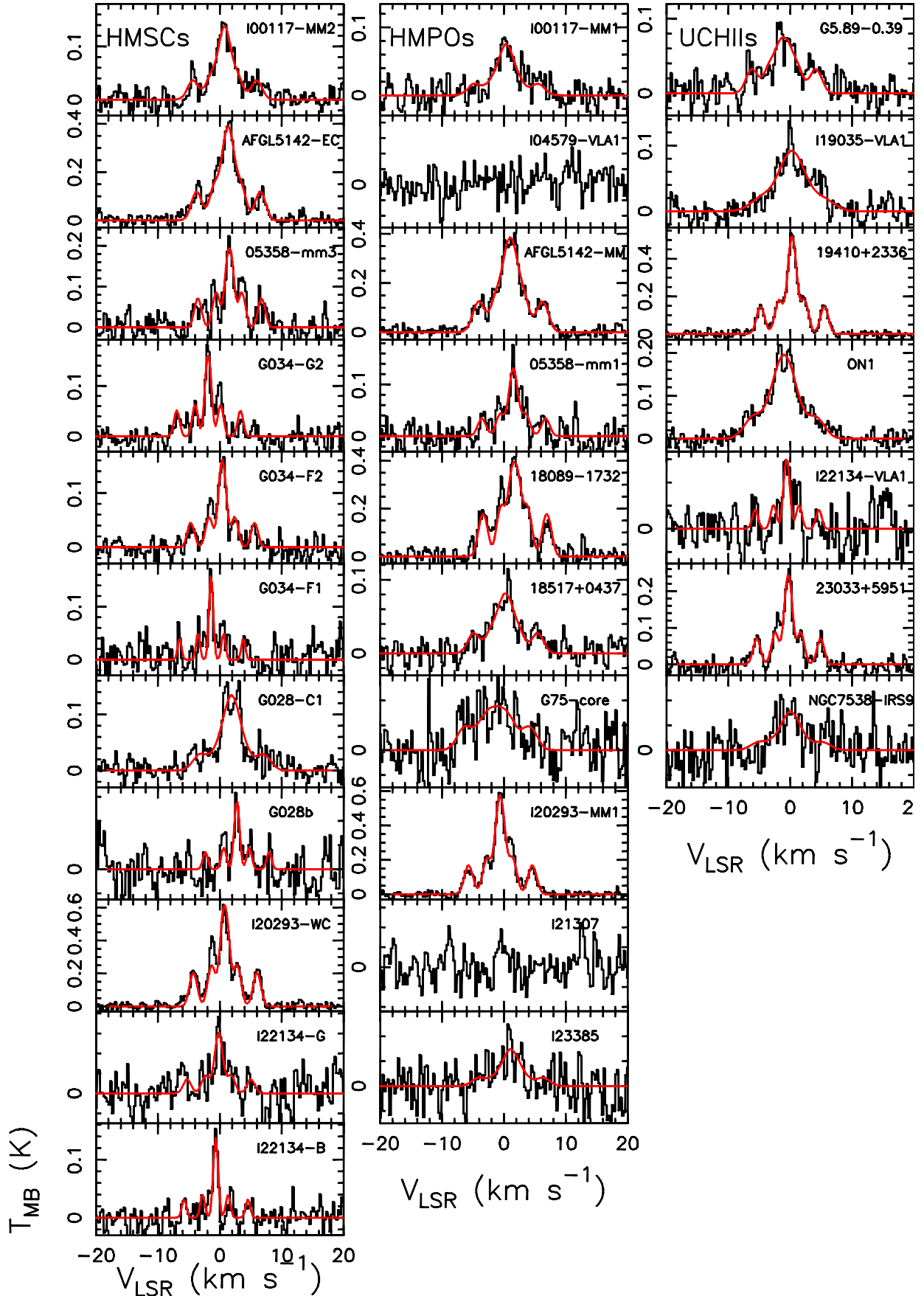


Fig. A-4. IRAM-30m spectra of *ortho*-NH₂D(1_{1,1} – 1_{0,1}) obtained towards all sources observed. We show the HMSCs in the left column, the HMPOs in the central column, and the UCHIIIs in the right column, from top to bottom in the same order as they appear in Table 1. For each spectrum, the x-axis represents a velocity interval of ± 20 km s⁻¹ from the systemic velocity listed in Table 1. The y-axis shows the intensity scale in main beam brightness temperature units. In each spectrum, the red curve indicates the best fit either obtained by fitting the hyperfine structure, when possible, or with a single Gaussian (see Sect. 3.1).

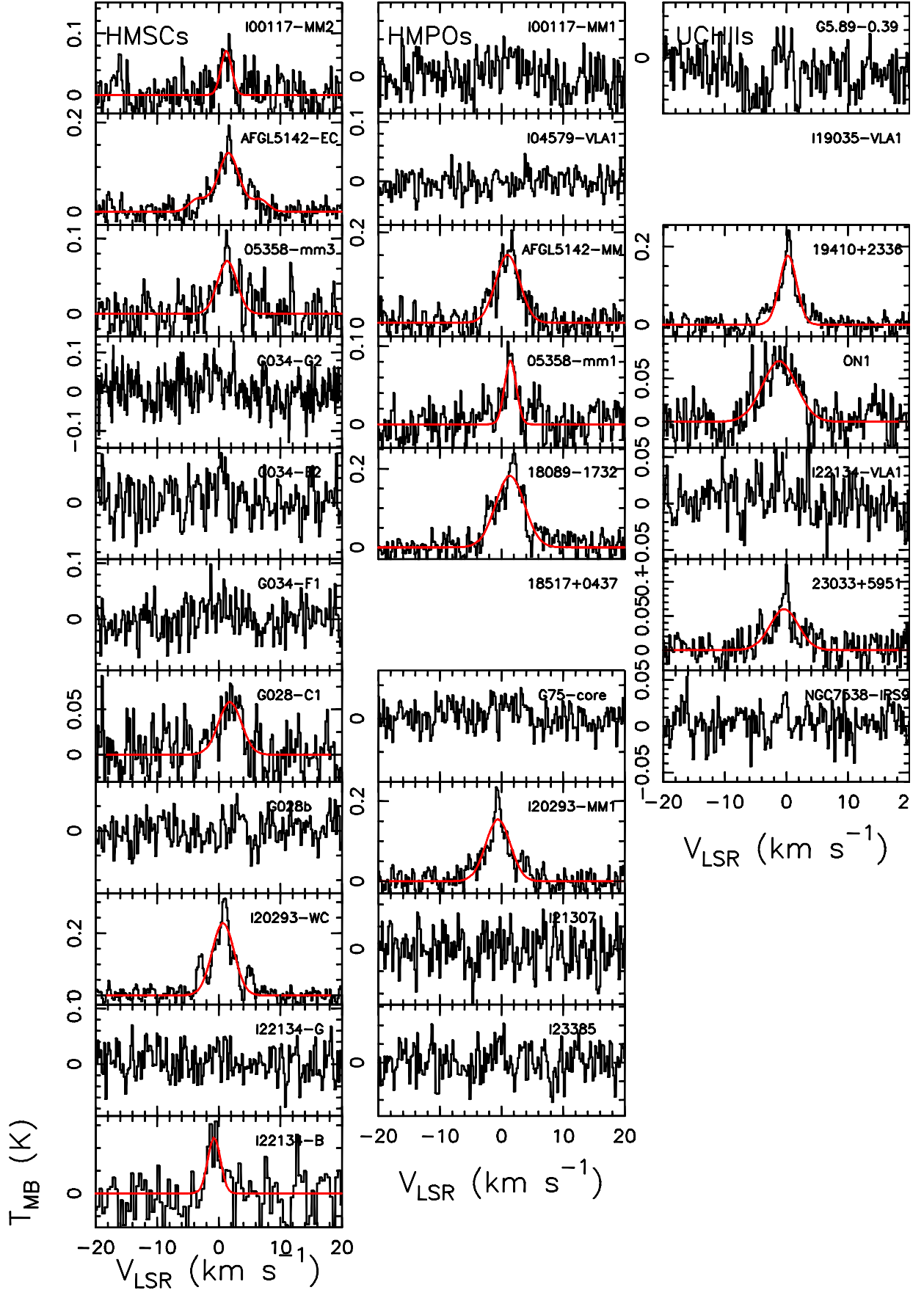


Fig. A-5. Same as Fig. A-4 for $\text{para-NH}_2\text{D}(1_{1,1} - 1_{0,1})$. Note that two sources (18517+0437 and I19035-VLA1) have not been observed. In each spectrum, the red curve indicates the best fit (see Sect. 3.1).

Appendix B: Tables

Table B-1. Transitions of CH₃OH, ¹³CH₃OH, CH₂DOH and CH₃OD detected at 3 mm, and line parameters derived from Gaussian fits: line integrated intensity ($\int T_{\text{MB}} dv$), full width at half maximum (ΔV) and main beam temperature at line peak (T_{pk}).

freq MHz	transition	$\int T_{\text{MB}} dv$ K km s ⁻¹	ΔV km s ⁻¹	T_{pk} K
HMSCs				
I00117-MM2				
94405.16	¹³ CH ₃ OH 2(-1,2)-1(-1,1)	0.014(0.004)	1.1(0.4)	0.012
95169.46	CH ₃ OH 8(0,8)-7(1,7)++	0.031(0.006)	2.4(0.5)	0.012
96739.36	CH ₃ OH 2(-1,2)-1(-1,1)	0.35(0.02)	0.7(0.2)	0.45131
96741.38	CH ₃ OH 2(0,2)-1(0,1)++	0.48(0.02)	0.7(0.2)	0.62447
96744.55	CH ₃ OH 2(0,2)-1(0,1)	0.06(0.02)	0.6(0.2)	0.09
96755.51	CH ₃ OH 2(1,1)-1(1,0)	0.02(0.01)	0.7(0.3)	0.02
AFGL5142-EC				
89505.78	CH ₃ OH 8(-4,5)-9(-3,7)	0.07(0.02)	1.9(0.8)	0.03
94405.16	¹³ CH ₃ OH 2(-1,2)-1(-1,1)	0.08(0.01)	1.5(0.2)	0.05
94407.13	¹³ CH ₃ OH 2(0,2)-1(0,1)++	0.06(0.02)	1.1(0.3)	0.06
94411.02	¹³ CH ₃ OH 2(0,2)-1(0,1)	0.04(0.03)	4.1(0.9)	0.01
94420.45	¹³ CH ₃ OH 2(1,1)-1(1,0)	0.014(0.007)	1.7(0.6)	0.01
94541.76	CH ₃ OH 8(3,5)-9(2,7)	0.083(0.009)	1.7(0.2)	0.05
95169.46	CH ₃ OH 8(0,8)-7(1,7)++	1.937(0.003)	1.1(0.4)	1.7
95914.31	CH ₃ OH 2(1,2)-1(1,1)++	0.6(0.2)	1.4(0.5)	0.4
96739.36	CH ₃ OH 2(-1,2)-1(-1,1)	4.3(0.1)	1.6(0.4)	2.6
96741.38	CH ₃ OH 2(0,2)-1(0,1)++	4.4(0.1)	2.0(0.4)	3.4
96744.55	CH ₃ OH 2(0,2)-1(0,1)	1.7(0.1)	1.9(0.4)	0.8
96755.51	CH ₃ OH 2(1,1)-1(1,0)	0.6(0.1)	1.413(0.4)	0.4
05358-mm3				
89407.91	CH ₂ DOH 2(0,2)-1(0,1)e0	0.020(0.006)	1.2(0.5)	0.02
91586.97	CH ₂ DOH 4(1,3)-4(0,4)	0.03(0.007)	1.7(0.6)	0.02
94405.16	¹³ CH ₃ OH 2(-1,2)-1(-1,1)	0.040(0.007)	1.0(0.2)	0.03
94407.13	¹³ CH ₃ OH 2(0,2)-1(0,1)++	0.101(0.009)	2.0(0.2)	0.05
94411.02	¹³ CH ₃ OH 2(0,2)-1(0,1)	0.008(0.003)	0.4(0.2)	0.02
94541.76	CH ₃ OH 8(3,5)-9(2,7)	0.021(0.006)	1.4(0.5)	0.02
95169.46	CH ₃ OH 8(0,8)-7(1,7)++	1.400(0.005)	0.839(0.004)	1.6
95914.31	CH ₃ OH 2(1,2)-1(1,1)++	0.33(0.04)	1.2(0.2)	0.25
96739.36	CH ₃ OH 2(-1,2)-1(-1,1)	2.4(0.1)	1.4(0.4)	1.7
96741.38	CH ₃ OH 2(0,2)-1(0,1)++	4.0(0.1)	1.6(0.4)	2.35
96744.55	CH ₃ OH 2(0,2)-1(0,1)	0.9(0.1)	1.5(0.4)	0.55
96755.51	CH ₃ OH 2(1,1)-1(1,0)	0.4(0.1)	1.6(0.4)	0.22
G034-G2				
89407.91	CH ₂ DOH 2(0,2)-1(0,1)e0	0.02(0.01)	0.8(0.2)	0.03
94405.16	¹³ CH ₃ OH 2(-1,2)-1(-1,1)	0.008(0.004)	1.0(0.4)	0.007
94407.13	¹³ CH ₃ OH 2(0,2)-1(0,1)++	0.010(0.003)	0.5(0.15)	0.018
96739.36	CH ₃ OH 2(-1,2)-1(-1,1)	0.764(0.004)	1.138(0.008)	0.63
96741.38	CH ₃ OH 2(0,2)-1(0,1)++	0.909(0.004)	1.009(0.005)	0.84
96744.55	CH ₃ OH 2(0,2)-1(0,1)	0.072(0.002)	0.91(0.05)	0.07
G034-F2				
96739.36	CH ₃ OH 2(-1,2)-1(-1,1)	0.37(0.02)	0.8(0.4)	0.46
96741.38	CH ₃ OH 2(0,2)-1(0,1)++	0.46(0.02)	0.8(0.4)	0.58
96744.55	CH ₃ OH 2(0,2)-1(0,1)	0.05(0.02)	1.4(0.4)	0.034
G034-F1				
95169.46	CH ₃ OH 8(0,8)-7(1,7)++	0.043(0.005)	1.3(0.2)	0.03
95914.31	CH ₃ OH 2(1,2)-1(1,1)++	0.035(0.009)	1.8(0.6)	0.02
96739.36	CH ₃ OH 2(-1,2)-1(-1,1)	0.65(0.025)	1.3(0.4)	0.46
96741.38	CH ₃ OH 2(0,2)-1(0,1)++	0.68(0.025)	1.2(0.4)	0.55
96744.55	CH ₃ OH 2(0,2)-1(0,1)	0.11(0.025)	1.7(0.4)	0.06
96755.51	CH ₃ OH 2(1,1)-1(1,0)	0.02(0.1)	1.7(0.9)	0.015
G028-C1				
94405.16	¹³ CH ₃ OH 2(-1,2)-1(-1,1)	0.013(0.003)	0.4(0.2)	0.03
94407.13	¹³ CH ₃ OH 2(0,2)-1(0,1)++	0.039(0.005)	0.9(0.1)	0.04
95169.46	CH ₃ OH 8(0,8)-7(1,7)++	0.033(0.015)	1.8(0.6)	0.017
96739.36	CH ₃ OH 2(-1,2)-1(-1,1)	0.94(0.04)	1.1(0.4)	0.84
96741.38	CH ₃ OH 2(0,2)-1(0,1)++	1.12(0.04)	1.0(0.4)	1.03
96744.55	CH ₃ OH 2(0,2)-1(0,1)	0.32(0.04)	2.9(0.4)	0.1
96755.51	CH ₃ OH 2(1,1)-1(1,0)	0.02(0.008)	0.9(0.4)	0.02
I20293-WC				
95169.46	CH ₃ OH 8(0,8)-7(1,7)++	0.205(0.005)	0.94(0.03)	0.2
95914.31	CH ₃ OH 2(1,2)-1(1,1)++	0.06(0.02)	2.3(0.9)	0.023
96739.36	CH ₃ OH 2(-1,2)-1(-1,1)	0.84(0.03)	1.6(0.4)	0.48

Table B-1. continued.

freq MHz	transition	$\int T_{\text{MB}} d\nu$ K km s ⁻¹	ΔV km s ⁻¹	T_{pk} K
96741.38	CH ₃ OH 2(0,2)–1(0,1)++	0.73(0.03)	1.0(0.4)	0.66
96744.55	CH ₃ OH 2(0,2)–1(0,1)	0.14(0.03)	1.4(0.4)	0.09
96755.51	CH ₃ OH 2(1,1)–1(1,0)	0.05(0.03)	1.6(0.4)	0.03
I22134–G				
95169.46	CH ₃ OH 8(0,8)–7(1,7)++	0.030(0.005)	1.1(0.2)	0.026
96739.36	CH ₃ OH 2(–1,2)–1(–1,1)	0.28(0.02)	0.8(0.4)	0.32
96741.38	CH ₃ OH 2(0,2)–1(0,1)++	0.39(0.02)	0.7(0.4)	0.49
96744.55	CH ₃ OH 2(0,2)–1(0,1)	0.06(0.02)	0.7(0.4)	0.08
96755.51	CH ₃ OH 2(1,1)–1(1,0)	0.02(0.02)	0.9(0.4)	0.02
I22134–B				
96739.36	CH ₃ OH 2(–1,2)–1(–1,1)	0.113(0.002)	0.60(0.02)	0.18
96741.38	CH ₃ OH 2(0,2)–1(0,1)++	0.157(0.002)	0.60(0.01)	0.25
96744.55	CH ₃ OH 2(0,2)–1(0,1)''	0.018(0.002)	0.57(0.07)	0.03
HMPOs				
I00117–MM1				
95169.46	CH ₃ OH 8(0,8)–7(1,7)++	0.024(0.005)	1.2(0.3)	0.02
96739.36	CH ₃ OH 2(–1,2)–1(–1,1)	0.23(0.01)	0.8(0.4)	0.27
96741.38	CH ₃ OH 2(0,2)–1(0,1)++	0.35(0.01)	0.8(0.4)	0.39
96744.55	CH ₃ OH 2(0,2)–1(0,1)	0.04(0.01)	0.7(0.4)	0.052
96755.51	CH ₃ OH 2(1,1)–1(1,0)	0.01(0.01)	0.8(0.9)	0.015
AFGL5142–MM				
89505.78	CH ₃ OH 8(–4,5)–9(–3,7)	0.08(0.05)	2.0(0.9)	0.04
91586.97	CH ₂ DOH 4(1,3)–4(0,4)	0.021(0.007)	1.4(0.4)	0.014
94405.16	¹³ CH ₃ OH 2(–1,2)–1(–1,1)	0.064(0.009)	1.3(0.2)	0.046
94407.13	¹³ CH ₃ OH 2(0,2)–1(0,1)++	0.09(0.01)	1.3(0.2)	0.06
94411.02	¹³ CH ₃ OH 2(0,2)–1(0,1)	0.015(0.007)	1.0(0.6)	0.014
94420.45	¹³ CH ₃ OH 2(1,1)–1(1,0)	0.006(0.007)	0.7(0.6)	0.008
94541.76	CH ₃ OH 8(3,5)–9(2,7)	0.10(0.01)	1.6(0.2)	0.055
95169.46	CH ₃ OH 8(0,8)–7(1,7)++	2.403(0.008)	0.935(0.004)	2.4
95914.31	CH ₃ OH 2(1,2)–1(1,1)++	0.71(0.06)	1.45(0.15)	0.46
96739.36	CH ₃ OH 2(–1,2)–1(–1,1)	4.0(0.15)	1.5(0.4)	2.45
96741.38	CH ₃ OH 2(0,2)–1(0,1)++	4.2(0.15)	1.3(0.4)	3.1
96744.55	CH ₃ OH 2(0,2)–1(0,1)	1.6(0.15)	1.7(0.4)	0.87
96755.51	CH ₃ OH 2(1,1)–1(1,0)	0.7(0.15)	1.6(0.4)	0.4
05358–mm1				
89505.78	CH ₃ OH 8(–4,5)–9(–3,7)	2.66615E-02(0.317)	1.751(125.117)	1.43062E-02
94405.16	¹³ CH ₃ OH 2(–1,2)–1(–1,1)	5.01113E-02(0.008)	1.129(0.184)	4.17009E-02
94407.13	¹³ CH ₃ OH 2(0,2)–1(0,1)++	5.25924E-02(0.010)	1.632(0.425)	3.02682E-02
95914.31	CH ₃ OH 2(1,2)–1(1,1)++	0.28432(0.035)	1.289(0.199)	0.20717
96739.36	CH ₃ OH 2(–1,2)–1(–1,1)	2.2854(0.107)	1.366(0.391)	1.5720
96741.38	CH ₃ OH 2(0,2)–1(0,1)++	3.7474(0.107)	1.615(0.391)	2.1795
96744.55	CH ₃ OH 2(0,2)–1(0,1)	0.91252(0.107)	1.713(0.391)	0.50046
96755.51	CH ₃ OH 2(1,1)–1(1,0)	0.33703(0.107)	1.605(0.391)	0.19726
95169.46	CH ₃ OH 8(0,8)–7(1,7)++	1.4000(0.006)	0.663(0.003)	1.9824
18089–1732				
89275.41	CH ₂ DOH 2(0,2)–1(0,1)e1	0.01(0.01)	0.7(0.3)	0.014
89505.78	CH ₃ OH 8(–4,5)–9(–3,7)	0.18(0.09)	1.4(0.8)	0.12
90384.31	¹³ CH ₃ OH 13(1,13)–12(2,10)	0.027(0.007)	1.4(0.4)	0.018
92588.70	¹³ CH ₃ OH 7(2,6)–8(1,7)–	0.030(0.007)	0.8(0.3)	0.034
93619.46	¹³ CH ₃ OH 2(1,2)–1(1,1)++	0.04(0.01)	1.4(0.4)	0.03
94405.16	¹³ CH ₃ OH 2(–1,2)–1(–1,1)	0.095(0.008)	1.8(0.2)	0.05
94407.13	¹³ CH ₃ OH 2(0,2)–1(0,1)++	0.084(0.007)	1.1(0.1)	0.07
94411.02	¹³ CH ₃ OH 2(0,2)–1(0,1)	0.072(0.005)	1.5(0.1)	0.04
94420.45	¹³ CH ₃ OH 2(1,1)–1(1,0)	0.048(0.005)	1.3(0.2)	0.03
94541.76	CH ₃ OH 8(3,5)–9(2,7)	0.230(0.006)	1.61(0.05)	0.13
94814.99	CH ₃ OH 19(7,13)–20(6,14)++	0.050(0.006)	1.4(0.2)	0.033
95169.46	CH ₃ OH 8(0,8)–7(1,7)++''	1.27(0.02)	1.2(0.4)	1.015
95208.66	¹³ CH ₃ OH 2(1,1)–1(1,0)–	0.06(0.02)	1.8(0.4)	0.029
95273.44	¹³ CH ₃ OH 6(–2,5)–7(–1,7)	0.05(0.02)	1.7(0.4)	0.027
95914.31	CH ₃ OH 2(1,2)–1(1,1)++	0.60(0.09)	1.4(0.3)	0.40
96739.36	CH ₃ OH 2(–1,2)–1(–1,1)	1.58(0.07)	1.3(0.4)	1.14
96741.38	CH ₃ OH 2(0,2)–1(0,1)++	1.95(0.07)	1.2(0.4)	1.5
96744.55	CH ₃ OH 2(0,2)–1(0,1)	0.87(0.07)	1.4(0.4)	0.58
96755.51	CH ₃ OH 2(1,1)–1(1,0)	0.57(0.07)	1.5(0.4)	0.36
18517+0437				
89505.78	CH ₃ OH 8(–4,5)–9(–3,7)	0.07(0.2)	1.5(0.4)	0.04

Table B-1. continued.

freq MHz	transition	$\int T_{\text{MB}} d\nu$ K km s ⁻¹	ΔV km s ⁻¹	T_{pk} K
94405.16	¹³ CH ₃ OH 2(-1,2)-1(-1,1)	0.055(0.004)	1.4(0.4)	0.04
94407.13	¹³ CH ₃ OH 2(0,2)-1(0,1)++	0.066(0.004)	1.1(0.4)	0.06
94411.02	¹³ CH ₃ OH 2(0,2)-1(0,1)	0.017(0.004)	1.0(0.4)	0.015
94541.76	CH ₃ OH 8(3,5)-9(2,7)	0.138(0.004)	2.0(0.4)	0.06
95169.46	CH ₃ OH 8(0,8)-7(1,7)++	0.648(0.003)	0.821(0.006)	0.74
95914.31	CH ₃ OH 2(1,2)-1(1,1)++	0.44(0.04)	1.3(0.1)	0.32
96739.36	CH ₃ OH 2(-1,2)-1(-1,1)	1.93(0.09)	1.2(0.4)	1.5
96741.38	CH ₃ OH 2(0,2)-1(0,1)++	2.70(0.09)	1.2(0.4)	2.12
96744.55	CH ₃ OH 2(0,2)-1(0,1)	0.85(0.09)	1.2(0.4)	0.64
96755.51	CH ₃ OH 2(1,1)-1(1,0)	0.46(0.09)	1.4(0.4)	0.31
G75-HCHII				
89505.78	CH ₃ OH 8(-4,5)-9(-3,7)	0.1(0.1)	0.9(0.8)	0.06
94405.16	¹³ CH ₃ OH 2(-1,2)-1(-1,1)	0.033(0.009)	1.6(0.5)	0.02
94407.13	¹³ CH ₃ OH 2(0,2)-1(0,1)++	0.025(0.008)	1.0(0.3)	0.024
94541.76	CH ₃ OH 8(3,5)-9(2,7)	0.074(0.005)	1.4(0.1)	0.05
95169.46	CH ₃ OH 8(0,8)-7(1,7)++	0.934(0.006)	1.98(0.02)	0.44
95914.31	CH ₃ OH 2(1,2)-1(1,1)++	0.37(0.06)	1.4(0.25)	0.26
96739.36	CH ₃ OH 2(-1,2)-1(-1,1)	1.13(0.06)	1.5(0.4)	0.70
96741.38	CH ₃ OH 2(0,2)-1(0,1)++	2.00(0.06)	1.7(0.4)	1.07
96744.55	CH ₃ OH 2(0,2)-1(0,1)	0.81(0.06)	1.8(0.4)	0.42
96755.51	CH ₃ OH 2(1,1)-1(1,0)	0.34(0.06)	1.3(0.4)	0.24
I20293-MM1				
94405.16	¹³ CH ₃ OH 2(-1,2)-1(-1,1)	0.033(0.008)	1.6(0.5)	0.02
94407.13	¹³ CH ₃ OH 2(0,2)-1(0,1)++	0.024(0.007)	0.7(0.2)	0.03
94541.76	CH ₃ OH 8(3,5)-9(2,7)	0.04(0.01)	5(1)	0.007
95169.46	CH ₃ OH 8(0,8)-7(1,7)++	1.387(0.007)	1.126(0.007)	1.16
95914.31	CH ₃ OH 2(1,2)-1(1,1)++	0.15(0.03)	1.5(0.4)	0.09
96739.36	CH ₃ OH 2(-1,2)-1(-1,1)	1.28(0.06)	1.2(0.4)	1.01
96741.38	CH ₃ OH 2(0,2)-1(0,1)++	1.81(0.06)	1.2(0.4)	1.4
96744.55	CH ₃ OH 2(0,2)-1(0,1)	0.81(0.06)	2.9(0.4)	0.26
96755.51	CH ₃ OH 2(1,1)-1(1,0)	0.12(0.06)	1.1(0.4)	0.1
I21307				
95169.46	CH ₃ OH 8(0,8)-7(1,7)++	0.201(0.004)	0.64(0.02)	0.3
95914.31	CH ₃ OH 2(1,2)-1(1,1)++	0.03(0.01)	1.2(0.6)	0.02
96739.36	CH ₃ OH 2(-1,2)-1(-1,1)	0.220(0.004)	0.84(0.02)	0.25
96741.38	CH ₃ OH 2(0,2)-1(0,1)++	0.321(0.004)	0.86(0.02)	0.35
96744.55	CH ₃ OH 2(0,2)-1(0,1)	0.080(0.005)	0.97(0.06)	0.08
96755.51	CH ₃ OH 2(1,1)-1(1,0)	0.026(0.004)	0.9(0.2)	0.03
I23385				
94405.16	¹³ CH ₃ OH 2(-1,2)-1(-1,1)	0.015(0.004)	0.9(0.2)	0.016
94407.13	¹³ CH ₃ OH 2(0,2)-1(0,1)++	0.013(0.004)	0.9(0.3)	0.013
95169.46	CH ₃ OH 8(0,8)-7(1,7)++	0.464(0.005)	1.15(0.02)	0.38
95914.31	CH ₃ OH 2(1,2)-1(1,1)++	0.11(0.02)	1.25(0.3)	0.08
96739.36	CH ₃ OH 2(-1,2)-1(-1,1)	0.77(0.04)	1.3(0.4)	0.57
96741.38	CH ₃ OH 2(0,2)-1(0,1)++	1.13(0.04)	1.3(0.4)	0.8
96744.55	CH ₃ OH 2(0,2)-1(0,1)	0.33(0.04)	1.8(0.4)	0.2
96755.51	CH ₃ OH 2(1,1)-1(1,0)	0.08(0.04)	0.75(0.4)	0.1
UC Hns				
G5.89-0.39				
94405.16	¹³ CH ₃ OH 2(-1,2)-1(-1,1)	0.050(0.004)	1.8(0.4)	0.025
94407.13	¹³ CH ₃ OH 2(0,2)-1(0,1)++	0.100(0.004)	2.0(0.4)	0.04
94411.02	¹³ CH ₃ OH 2(0,2)-1(0,1)	0.03(0.004)	1.0(0.4)	0.03
94420.45	¹³ CH ₃ OH 2(1,1)-1(1,0)	0.011(0.004)	1.3(0.4)	0.01
94541.76	CH ₃ OH 8(3,5)-9(2,7)	0.052(0.004)	1.4(0.4)	0.03
95169.46	CH ₃ OH 8(0,8)-7(1,7)++	2.726(0.007)	1.638(0.007)	1.56
95914.31	CH ₃ OH 2(1,2)-1(1,1)++	0.97(0.05)	1.8(0.1)	0.49
96739.36	CH ₃ OH 2(-1,2)-1(-1,1)	3.8(0.1)	2.5(0.4)	1.43
96741.38	CH ₃ OH 2(0,2)-1(0,1)++	2.4(0.1)	1.4(0.4)	1.66
96744.55	CH ₃ OH 2(0,2)-1(0,1)	1.6(0.1)	1.8(0.4)	0.83
96755.51	CH ₃ OH 2(1,1)-1(1,0)	0.9(0.1)	1.9(0.4)	0.47
II9035-VLA1				
94407.13	¹³ CH ₃ OH 2(0,2)-1(0,1)++	0.032(0.005)	1.2(0.2)	0.024
94411.02	¹³ CH ₃ OH 2(0,2)-1(0,1)	0.008(0.003)	0.4(0.3)	0.02
94420.45	¹³ CH ₃ OH 2(1,1)-1(1,0)	0.014(0.006)	2.0(0.8)	0.007
94541.76	CH ₃ OH 8(3,5)-9(2,7)	0.033(0.009)	4(1)	0.008
95169.46	CH ₃ OH 8(0,8)-7(1,7)++	0.147(0.007)	1.9(0.1)	0.07

Table B-1. continued.

freq MHz	transition	$\int T_{\text{MB}} d\nu$ K km s ⁻¹	ΔV km s ⁻¹	T_{pk} K
95914.31	CH ₃ OH 2(1,2)–1(1,1)++	0.12(0.02)	1.7(0.4)	0.065
96739.36	CH ₃ OH 2(–1,2)–1(–1,1)	0.98(0.045)	1.5(0.4)	0.62
96741.38	CH ₃ OH 2(0,2)–1(0,1)++	1.70(0.045)	1.8(0.4)	0.89
96744.55	CH ₃ OH 2(0,2)–1(0,1)	0.52(0.045)	2.1(0.4)	0.23
96755.51	CH ₃ OH 2(1,1)–1(1,0)	0.17(0.045)	1.9(0.4)	0.08
19410+2336				
94405.16	¹³ CH ₃ OH 2(–1,2)–1(–1,1)	0.026(0.004)	0.9(0.2)	0.03
94407.13	¹³ CH ₃ OH 2(0,2)–1(0,1)++	0.044(0.004)	1.0(0.1)	0.04
94541.76	CH ₃ OH 8(3,5)–9(2,7)	0.028(0.005)	1.6(0.4)	0.016
95169.46	CH ₃ OH 8(0,8)–7(1,7)++	1.014(0.004)	0.641(0.003)	1.49
95914.31	CH ₃ OH 2(1,2)–1(1,1)++	0.24(0.05)	1.0(0.3)	0.22
96739.36	CH ₃ OH 2(–1,2)–1(–1,1)	1.56(0.08)	1.0(0.4)	1.51
96741.38	CH ₃ OH 2(0,2)–1(0,1)++	2.32(0.08)	1.0(0.4)	2.16
96744.55	CH ₃ OH 2(0,2)–1(0,1)	0.61(0.08)	1.0(0.4)	0.57
96755.51	CH ₃ OH 2(1,1)–1(1,0)	0.21(0.08)	0.8(0.4)	0.27
ON1				
94405.16	¹³ CH ₃ OH 2(–1,2)–1(–1,1)	0.048(0.009)	1.5(0.2)	0.03
94407.13	¹³ CH ₃ OH 2(0,2)–1(0,1)++	0.11(0.01)	1.9(0.2)	0.053
94411.02	¹³ CH ₃ OH 2(0,2)–1(0,1)	0.010(0.004)	0.9(0.5)	0.011
94420.45	¹³ CH ₃ OH 2(1,1)–1(1,0)	0.014(0.005)	2.3(0.8)	0.006
94541.76	CH ₃ OH 8(3,5)–9(2,7)	0.065(0.004)	1.3(0.1)	0.047
95169.46	CH ₃ OH 8(0,8)–7(1,7)++	0.730(0.007)	0.97(0.01)	0.70
95914.31	CH ₃ OH 2(1,2)–1(1,1)++	0.39(0.04)	1.8(0.2)	0.21
96739.36	CH ₃ OH 2(–1,2)–1(–1,1)	2.1(0.1)	1.3(0.4)	1.48
96741.38	CH ₃ OH 2(0,2)–1(0,1)++	3.9(0.1)	1.8(0.4)	2.01
96744.55	CH ₃ OH 2(0,2)–1(0,1)	1.3(0.1)	2.2(0.4)	0.55
96755.51	CH ₃ OH 2(1,1)–1(1,0)	0.5(0.1)	1.9(0.4)	0.23
I22134–VLA1				
95169.46	CH ₃ OH 8(0,8)–7(1,7)++	0.022(0.003)	0.7(0.1)	0.03
95914.31	CH ₃ OH 2(1,2)–1(1,1)++	0.02(0.02)	1.4(0.9)	0.01
96739.36	CH ₃ OH 2(–1,2)–1(–1,1)	0.23(0.01)	0.9(0.4)	0.25
96741.38	CH ₃ OH 2(0,2)–1(0,1)++	0.30(0.01)	0.744(0.4)	0.38
96744.55	CH ₃ OH 2(0,2)–1(0,1)	0.06(0.01)	0.7(0.4)	0.085
96755.51	CH ₃ OH 2(1,1)–1(1,0)	0.01(0.01)	0.5(0.4)	0.026
23033+5951				
94405.16	¹³ CH ₃ OH 2(–1,2)–1(–1,1)	0.022(0.005)	1.2(0.3)	0.017
94407.13	¹³ CH ₃ OH 2(0,2)–1(0,1)++	0.034(0.004)	1.2(0.3)	0.026
95169.46	CH ₃ OH 8(0,8)–7(1,7)++	0.634(0.003)	0.647(0.004)	0.92
95914.31	CH ₃ OH 2(1,2)–1(1,1)++	0.09(0.03)	1.1(0.5)	0.07
96739.36	CH ₃ OH 2(–1,2)–1(–1,1)	1.59(0.07)	1.1(0.4)	1.33
96741.38	CH ₃ OH 2(0,2)–1(0,1)++	1.94(0.07)	1.0(0.4)	1.75
96744.55	CH ₃ OH 2(0,2)–1(0,1)	0.32(0.07)	1.0(0.4)	0.31
96755.51	CH ₃ OH 2(1,1)–1(1,0)	0.1(0.2)	1.1(0.9)	0.09
NGC7538–IRS9				
94405.16	¹³ CH ₃ OH 2(–1,2)–1(–1,1)	0.020(0.004)	1.1(0.3)	0.02
94407.13	¹³ CH ₃ OH 2(0,2)–1(0,1)++	0.019(0.004)	0.7(0.2)	0.03
95169.46	CH ₃ OH 8(0,8)–7(1,7)++	0.904(0.003)	0.737(0.002)	1.15
95914.31	CH ₃ OH 2(1,2)–1(1,1)++	0.15(0.03)	1.1(0.2)	0.13
96739.36	CH ₃ OH 2(–1,2)–1(–1,1)	0.95(0.05)	1.2(0.4)	0.77
96741.38	CH ₃ OH 2(0,2)–1(0,1)++	1.67(0.05)	1.5(0.4)	1.06
96744.55	CH ₃ OH 2(0,2)–1(0,1)	0.46(0.05)	1.6(0.4)	0.28
96755.51	CH ₃ OH 2(1,1)–1(1,0)	0.17(0.05)	1.4(0.4)	0.11

Table B-2. Same as Table B-1 for the transitions detected at 1 mm.

freq MHz	transition	$\int T_{\text{MB}} dv$ K km s ⁻¹	ΔV km s ⁻¹	T_{pk} K
HMSCs				
I00117-MM2				
218440.05	CH ₃ OH 4(2,2)–3(1,2)	0.29(0.03)	1.9(0.2)	0.14
AFGL5142-EC				
216945.6	CH ₃ OH 5(1,4)–4(2,2)	1.9(0.3)	3.3(0.6)	0.53
218440.05	CH ₃ OH 4(2,2)–3(1,2)	10.1(0.4)	2.9(0.1)	3.23
220078.5	CH ₃ OH 8(0,8)–7(1,6)	2(1)	3.7(0.9)	0.59
223071.3	CH ₂ DOH 5(2,3)–4(1,4)e1	0.02(0.01)	0.4(0.8)	0.06
223107.3	CH ₂ DOH 5(0,5)–4(0,4)o1	0.03(0.02)	0.6(0.3)	0.04
223153.7	CH ₂ DOH 5(3,2)–4(3,1)o1	0.06(0.03)	2.1(0.7)	0.03
223315.4	CH ₂ DOH 5(2,3)–4(2,2)e1	0.05(0.02)	2.0(0.7)	0.024 ^a
223422.3	CH ₂ DOH 5(2,4)–4(2,3)e0	0.09(0.02)	2.6(0.6)	0.032 ^a
05358-mm3				
216945.60	CH ₃ OH 5(1,4)–4(2,2)	0.67(0.06)	2.2(0.3)	0.29
218440.05	CH ₃ OH 4(2,2)–3(1,2)	5.1(0.2)	1.96(0.08)	2.46
220078.49	CH ₃ OH 8(0,8)–7(1,6)	0.8(0.4)	2(1)	0.32
G034-G2				
218440.05	CH ₃ OH 4(2,2)–3(1,2)	0.11(0.02)	2.4(0.6)	0.045
G034-F2				
–	–	–	–	–
G034-F1				
218440.05	CH ₃ OH 4(2,2)–3(1,2)	0.10(0.02)	2.100(0.001)	0.043
G028-C1				
218440.05	CH ₃ OH 4(2,2)–3(1,2)	0.09(0.014)	1.188(0.001)	0.074
I20293-WC				
218440.05	CH ₃ OH 4(2,2)–3(1,2)	0.05(0.015)	2.0(0.7)	0.024
I22134-G				
218440.05	CH ₃ OH 4(2,2)–3(1,2)	0.23(0.02)	1.1(0.1)	0.20
I22134-B				
218440.05	CH ₃ OH 4(2,2)–3(1,2)	0.06(0.02)	2.1(0.7)	0.03
HMPOs				
I00117-MM1				
218440.05	CH ₃ OH 4(2,2)–3(1,2)	0.19(0.02)	1.9(0.3)	0.10
AFGL5142-MM				
216945.60	CH ₃ OH 5(1,4)–4(2,2)	1.9(0.2)	3.2(0.5)	0.55
217886.39	CH ₃ OH 20(1,19)–20(0,20)	0.59(0.06)	5.8(0.7)	0.09
218440.05	CH ₃ OH 4(2,2)–3(1,2)	9.9(0.4)	2.7(0.1)	3.46
219983.99	CH ₃ OH 25(3,22)–24(4,20)	0.10(0.09)	2.7(0.6)	0.037
219993.94	CH ₃ OH 23(5,19)–22(6,17)	0.04(0.03)	1.7(0.5)	0.02
220078.49	CH ₃ OH 8(0,8)–7(1,6)	2(1)	3(1)	0.6
223071.3	CH ₂ DOH 5(2,3)–4(1,4)e1	0.06(0.02)	1.6(0.7)	0.034 ^a
223308.57	CH ₃ OD 5(1,5)–4(1,4)A++	0.08(0.02)	1.4(0.4)	0.05 ^a
05358-mm1				
216945.60	CH ₃ OH 5(1,4)–4(2,2)	0.92(0.07)	3.3(0.4)	0.26
217886.39	CH ₃ OH 20(1,19)–20(0,20)	0.25(0.08)	8(2)	0.03
218440.05	CH ₃ OH 4(2,2)–3(1,2)	4.6(0.2)	2.5(0.2)	1.75
220078.49	CH ₃ OH 8(0,8)–7(1,6)	1.0(0.4)	3(1)	0.33
18089-1732				
216945.60	CH ₃ OH 5(1,4)–4(2,2)	3.3(0.2)	3.5(0.2)	0.89
217399.54	¹³ CH ₃ OH 10(2,8)–9(3,7)A++	0.96(0.08)	4.4(0.4)	0.20
217886.39	CH ₃ OH 20(1,19)–20(0,20)	1.39(0.08)	3.8(0.3)	0.34
218440.05	CH ₃ OH 4(2,2)–3(1,2)	8.6(0.3)	3.3(0.1)	2.44
219983.99	CH ₃ OH 25(3,22)–24(4,20)	0.4(0.6)	3.6(0.9)	0.09
219993.94	CH ₃ OH 23(5,19)–22(6,17)	0.4(0.6)	4.0(0.9)	0.09
220078.49	CH ₃ OH 8(0,8)–7(1,6)	3.7(0.7)	3.7(0.8)	0.93
223071.3	CH ₂ DOH 5(2,3)–4(1,4)e1	0.08(0.06)	2.4(0.3)	0.03
223107.3	CH ₂ DOH 5(0,5)–4(0,4)o1	0.08(0.06)	1.3(0.5)	0.057
223153.7	CH ₂ DOH 5(3,2)–4(3,1)o1	0.07(0.06)	1.0(0.5)	0.06
222468.34	¹³ CH ₃ OH 21(1,20)–21(0,21)	0.06(0.1)	1.7(0.5)	0.03
223308.57	CH ₃ OD 5(1,5)–4(1,4)A++	0.21(0.06)	2.6(0.7)	0.08 ^b
223315.4	CH ₂ DOH 5(2,3)–4(2,2)e1	0.06(0.04)	1.2(0.7)	0.05
18517+0437				
216945.60	CH ₃ OH 5(1,4)–4(2,2)	2.3(0.2)	3.6(0.3)	0.59
217886.39	CH ₃ OH 20(1,19)–20(0,20)	0.97(0.07)	4.6(0.4)	0.20
218440.05	CH ₃ OH 4(2,2)–3(1,2)	5.8(0.3)	2.7(0.2)	2.0
219983.99	CH ₃ OH 25(3,22)–24(4,20)	0.14(0.09)	3.8(0.8)	0.034

Table B-2. continued.

freq MHz	transition	$\int T_{\text{MB}} dv$ K km s ⁻¹	ΔV km s ⁻¹	T_{pk} K
219993.94	CH ₃ OH 23(5,19)–22(6,17)	0.13(0.09)	3.3(0.5)	0.038
220078.49	CH ₃ OH 8(0,8)–7(1,6)	2.1(0.7)	3.9(0.9)	0.52
221285.24	¹³ CH ₃ OH 8(–1,8)–7(0,7)	0.39(0.03)	3.8(0.3)	0.095
G75–HCHII				
216945.60	CH ₃ OH 5(1,4)–4(2,2)	2.3(0.2)	3.1(0.2)	0.69
217399.54	¹³ CH ₃ OH 10(2,8)–9(3,7)A++	0.57(0.06)	2.7(0.4)	0.20
217886.39	CH ₃ OH 20(1,19)–20(0,20)	0.45(0.06)	3.0(0.5)	0.14
218440.05	CH ₃ OH 4(2,2)–3(1,2)	6.4(0.3)	3.1(0.2)	1.92
220078.49	CH ₃ OH 8(0,8)–7(1,6)	2.2(0.8)	3.1(0.9)	0.66
223107.3	CH ₂ DOH 5(0,5)–4(0,4)o1	0.07(0.03)	2.2(0.9)	0.03
223422.3	CH ₂ DOH 5(2,4)–4(2,3)e0	0.04(0.02)	0.8(0.3)	0.05
I20293–MMI				
216945.60	CH ₃ OH 5(1,4)–4(2,2)	0.18(0.06)	2.9(0.9)	0.06
218440.05	CH ₃ OH 4(2,2)–3(1,2)	0.22(0.03)	2.7(0.4)	0.075
220078.49	CH ₃ OH 8(0,8)–7(1,6)	0.4(0.2)	5.4(0.9)	0.06
I21307				
216945.60	CH ₃ OH 5(1,4)–4(2,2)	0.10(0.02)	1.9(0.4)	0.05
218440.05	CH ₃ OH 4(2,2)–3(1,2)	0.99(0.05)	2.0(0.1)	0.47
220078.49	CH ₃ OH 8(0,8)–7(1,6)	0.1(0.2)	2.5(0.9)	0.04
I23385				
216945.60	CH ₃ OH 5(1,4)–4(2,2)	0.22(0.04)	3.0(0.8)	0.07
218440.05	CH ₃ OH 4(2,2)–3(1,2)	1.9(0.07)	2.7(0.1)	0.66
220078.49	CH ₃ OH 8(0,8)–7(1,6)	0.3(0.2)	3.2(0.9)	0.08
UC Hns				
G5.89–0.39				
216945.60	CH ₃ OH 5(1,4)–4(2,2)	4(1)	5(1)	0.82
217886.39	CH ₃ OH 20(1,19)–20(0,20)	0.08(0.08)	3.7(0.6)	0.02
218440.05	CH ₃ OH 4(2,2)–3(1,2)	20(2)	4.8(0.7)	3.87
220078.49	CH ₃ OH 8(0,8)–7(1,6)	5.3(0.8)	4.8(0.7)	1.04
221285.24	¹³ CH ₃ OH 8(–1,8)–7(0,7)	0.35(0.05)	4.8(0.8)	0.07
I19035–VLA1				
216945.60	CH ₃ OH 5(1,4)–4(2,2)	0.50(0.05)	4.2(0.5)	0.11
218440.05	CH ₃ OH 4(2,2)–3(1,2)	2.01(0.07)	3.6(0.15)	0.52
220078.49	CH ₃ OH 8(0,8)–7(1,6)	0.6(0.3)	5.0(0.9)	0.12
19410+2336				
216945.60	CH ₃ OH 5(1,4)–4(2,2)	0.55(0.04)	3.3(0.3)	0.16
218440.05	CH ₃ OH 4(2,2)–3(1,2)	0.38(0.02)	2.1(0.2)	0.17
220078.49	CH ₃ OH 8(0,8)–7(1,6)	0.6(0.4)	3.8(0.9)	0.14
ON1				
216945.60	CH ₃ OH 5(1,4)–4(2,2)	1.0(0.1)	3.6(0.5)	0.25
218440.05	CH ₃ OH 4(2,2)–3(1,2)	0.44(0.03)	3.1(0.2)	0.14
220078.49	CH ₃ OH 8(0,8)–7(1,6)	1.1(0.6)	4.2(0.9)	0.25
221285.24	¹³ CH ₃ OH 8(–1,8)–7(0,7)	0.12(0.02)	3.4(0.6)	0.033
I22134–VLA1				
218440.05	CH ₃ OH 4(2,2)–3(1,2)	0.23(0.03)	1.4(0.2)	0.16
220078.49	CH ₃ OH 8(0,8)–7(1,6)	0.03(0.05)	1.1(0.7)	0.03
23033–UCHII				
216945.60	CH ₃ OH 5(1,4)–4(2,2)	0.21(0.04)	2.9(0.7)	0.07
218440.05	CH ₃ OH 4(2,2)–3(1,2)	1.49(0.06)	2.3(0.1)	0.6
220078.49	CH ₃ OH 8(0,8)–7(1,6)	0.3(0.3)	4.7(0.9)	0.06
NGC7538–IRS9				
216945.60	CH ₃ OH 5(1,4)–4(2,2)	0.45(0.04)	3.1(0.3)	0.14
218440.05	CH ₃ OH 4(2,2)–3(1,2)	2.42(0.09)	2.4(0.1)	0.94
220078.49	CH ₃ OH 8(0,8)–7(1,6)	0.5(0.3)	3.3(0.9)	0.15

^a tentative detection in between 2 and 3 σ rms;^b partially blended with (CH₂OH)₂ (ethylene-glycol).